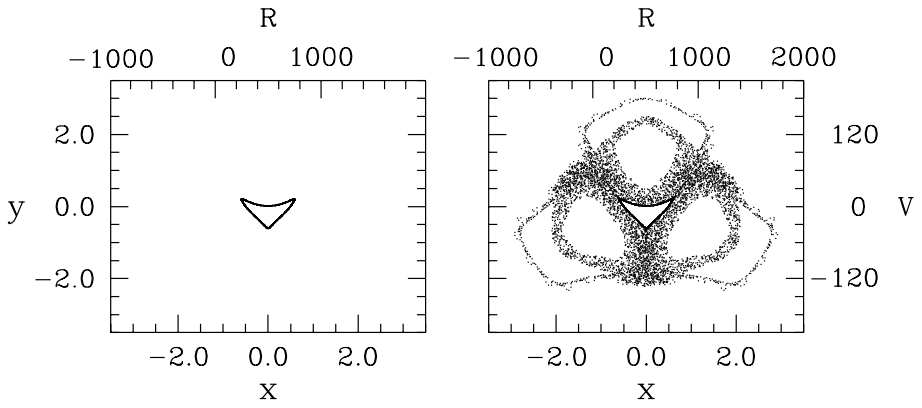

Figure 3.17: Poincaré map for the orbit of Figure 3.16. Panel *(a)* includes the points $R(\tau)$ and $V(\tau)$ for the time interval (1000-1400) years, whereas panel *(b)* shows the points $R(t)$ and $V(t)$ for the time interval (1000-2000) years.

This example corroborates the suggestion, first proposed by Buchler et al. (1977) and later found in the very detailed numerical calculations of Ya'ari & Tuchman (1996), that the long-term effects in Mira variables have an important role in understanding the mechanism which drives mass-loss. This result also argues in favor of the capability of simple models to "catch" the underlying dynamics of the physical system. To put it in a different way, these models, despite their simplicity, reproduce reasonably well the results obtained with full, sophisticated and nonlinear hydrodynamical models. It is nevertheless important to realize here that our model does not incorporate the secular effects induced by the thermal changes and, hence, it is quite likely that this kind of behavior is intrinsically associated to the physical characteristics of the oscillations of real stars. We shall come back to this behavior in the next section.

Following the evolution as the parameter α is slightly varied we find another interesting orbit of the system, which is represented for a particular initial condition in the lower panels of Figure 3.18. The Poincaré map is also shown in the top panel and illustrates how the main deformed torus breaks into several small pieces. In Figure 3.19 we present the velocity variations of a typical orbit from the stochastic sea. It suggests the necessity of a time-frequency analysis, which will be done in the next section. The classical approach of time-series analysis applied to this non-steady cases generally yields poor results. Nonlinear time-series analysis as well as time-frequency analysis are, thus, compulsory for these cases. Nevertheless, let us say at this point that, again, Figure 3.19 shows that the velocity of the outermost layers of the star reach quite frequently the escape velocity and, hence, mass-loss is most likely. Moreover, the fraction of time during which the outer layers of the model star have velocities in excess of the escape velocity is larger in this case than in the case of Figure 3.16. Thus, the more chaotic is the behavior of our simple linear model, the stronger is the mass-loss.

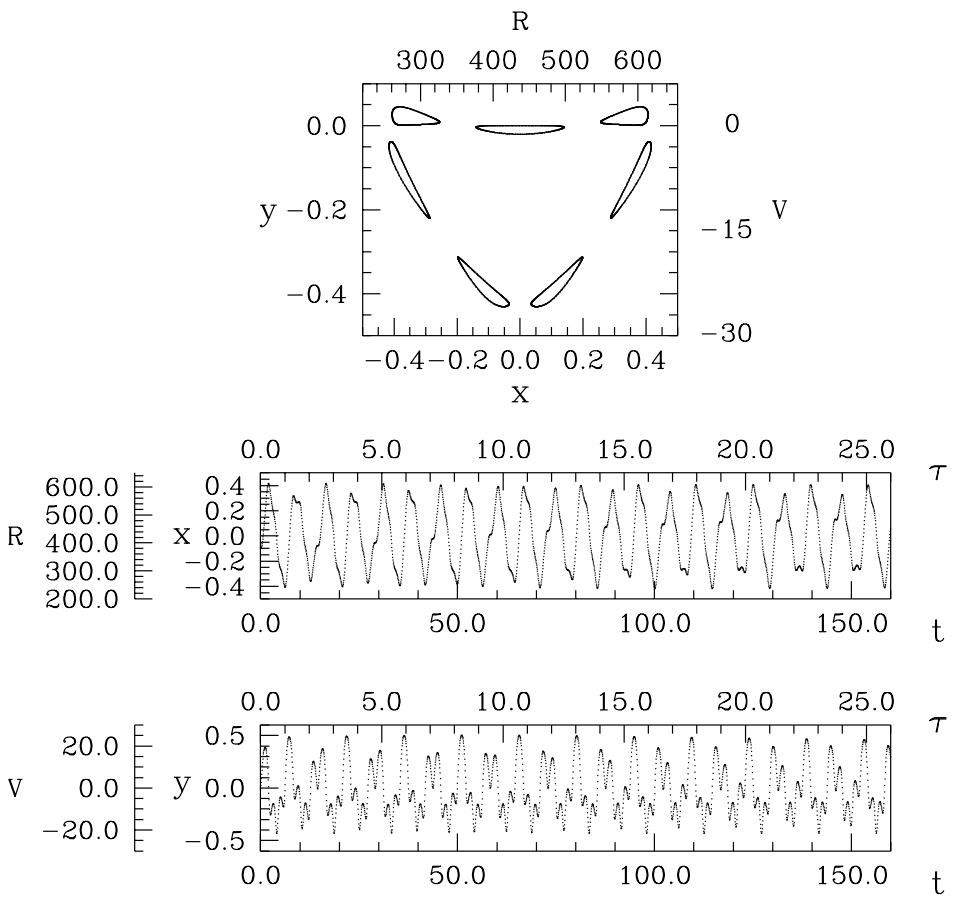

Figure 3.18: Poincaré map *(top)* for $\omega \simeq 3$, $\alpha = 0.35$, $\epsilon = 0.5$, and graph of $R(t)$ *(middle)* and $V(t)$ *(bottom)* for the initial condition $(x_0, y_0) = (-0.1, 0.0)$.

3.4 Time-frequency analysis

3.4.1 Description of the most usual methods

First of all, it has to be pointed out that the time-frequency analysis corresponds to a linear approach. It is of a purely interpolative nature and therefore does not provide any information about the nonlinear physical nature of the source of the time series. In contrast, the flow reconstruction method and the topological method are two recently developed tools specifically tailored to better understand intrinsically nonlinear time-series or models (Buchler & Kolláth 2001). However, since our model is basically a perturbed linear oscillator, the time-frequency analysis is perfectly appropriate for the study of the non-steady resultant time-series. The most classical tool used in time-frequency analysis is the so called short-time Fourier transform (STFT), which is also frequently referred to as the windowed Fourier transform. The

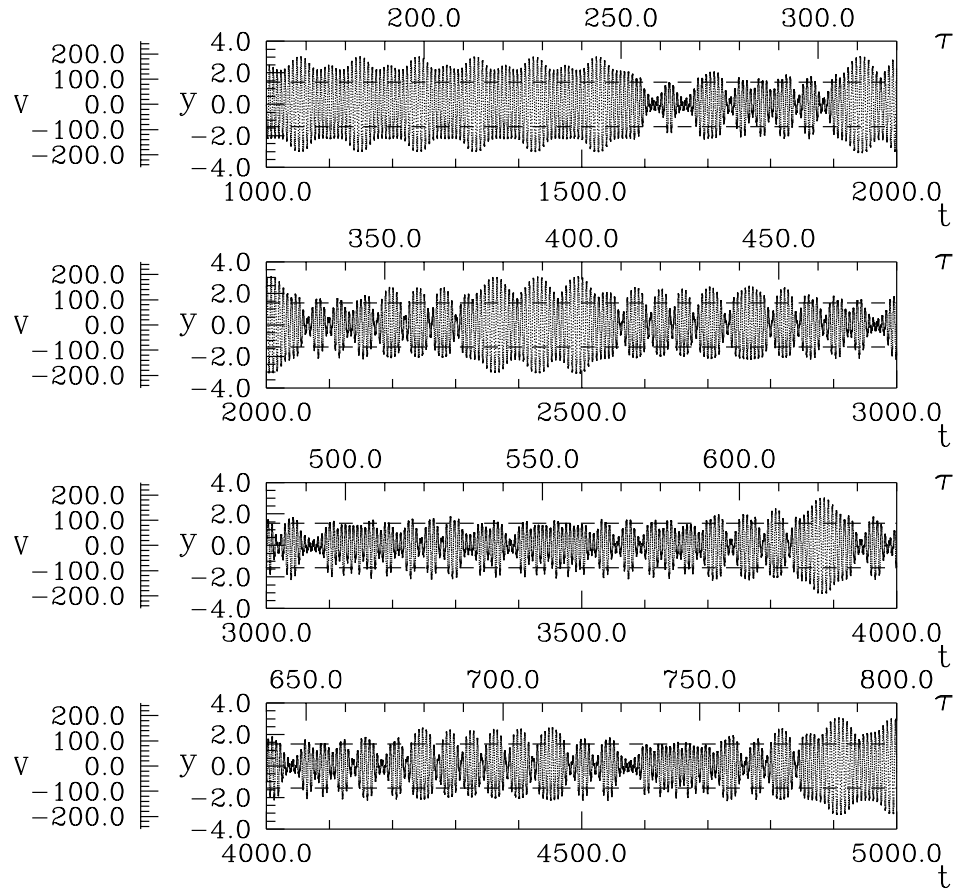

Figure 3.19: Velocity variations for the case of $\alpha = 0.2, \epsilon = 0.5$ and nondimensional initial condition $(x_0, y_0) = (-0.1, 0.0)$. The escape velocity ($v_{\text{esc}} \simeq 86$ km/s) is represented as a dashed line.

signal $s(t)$ is weighted by a time-localized window function $h(t)$ and then Fourier transformed:

$$F(t,\nu) = \int_{-\infty}^{+\infty} s(\tau) h^*(\tau - t) e^{-2i\pi\tau\nu} d\tau. \tag{3.13}$$

The STFT was first introduced in Gábor (1946) with the Gaussian analyzing window:

$$h(t) = e^{-t^2/(2\tau^2)}. \tag{3.14}$$

This time-frequency analysis is generally referred to as the Gábor transform (GT). The spectrogram is the power spectrum version, $|F(t,\nu)|^2$, of the STFT. The generalized form of the time-frequency distributions (GTFD) was introduced in Cohen (1966) — see also Cohen (1995) — and it is :

$$C(t,\nu) = \frac{1}{2\pi}\int\int\int e^{-i\theta t - 2i\pi\tau\nu + i\tau u}\,\Phi(\theta,\tau)z^*\left(u-\frac{\tau}{2}\right)z\left(u+\frac{\tau}{2}\right)dud\tau d\theta, \tag{3.15}$$

where $z(t)$ is the complex signal associated to the real one, $s(t)$, and $\Phi(\theta,\tau)$ is the so-called kernel of the distribution. Most practical signals are purely real, which implies the existence of a negative frequency component in the associated Fourier analysis. This property introduces undesirable cross-terms in the associated time-frequency diagrams. The complex (or analytic) signal, $z(t)$ is generated by suppressing the negative frequency components while preserving the positive components:

$$z(t) = \frac{1}{2\pi^{1/2}}\int_{-\infty}^{+\infty} s(\nu)e^{i\nu t}d\nu, \tag{3.16}$$

where $s(\nu)$ are the coefficients of the Fourier transform for the real signal at frequency ν. It can be easily shown that with the simplest kernel, $\Phi(\theta,\tau) = 1$, the definition of the GTFD reduces to the so-called Wigner-Ville distribution (WVD):

$$W(t,\nu) = \int e^{-2i\pi\tau\nu}z^*\left(t-\frac{\tau}{2}\right)z\left(t+\frac{\tau}{2}\right)d\tau. \tag{3.17}$$

To avoid the problem of undesired cross-terms in the distribution, one can also use a kernel with localizing properties. One of such kernels was defined by Choi & Williams (1989), i.e., $\Phi(\theta,\tau) = \exp(-\theta^2\tau^2/\tau)$, and gives the following distribution:

$$C(t,\nu) = \frac{1}{2\pi^{1/2}}\int\int \frac{1}{\sqrt{\tau^2\sigma}}e^{-\sigma(u-t)^2/\tau^2 - 2i\pi\tau\nu}z^*\left(u-\frac{\tau}{2}\right)z\left(u+\frac{\tau}{2}\right)dud\tau. \tag{3.18}$$

Is is straightforward to show that the Gábor transform is obtained from the distribution of Eq.(3.15) with the kernel

$$\Phi(\theta,\tau) = e^{-\tau^2/(4\sigma^2)-\sigma^2\theta^2}. \tag{3.19}$$

3.4.2 Results

The different forms of frequency spectra (mainly the Fourier transform) became an important tool for the analysis of multiperiodic variations, and the Fourier decomposition of the periodic light curves of Cepheids and RR Lyrae stars turned into a powerful device for the comparison of observations and theoretical models. Kolláth & Buchler (1997) compared the results obtained with different time-frequency methods using both real light-curves and synthetic signals and from these tests they concluded that the Gábor transform provides much more informative results on the high frequency part of the data than the wavelet transform, and that the time-frequency analysis using the Choi-Williams distribution is definitely superior to both methods

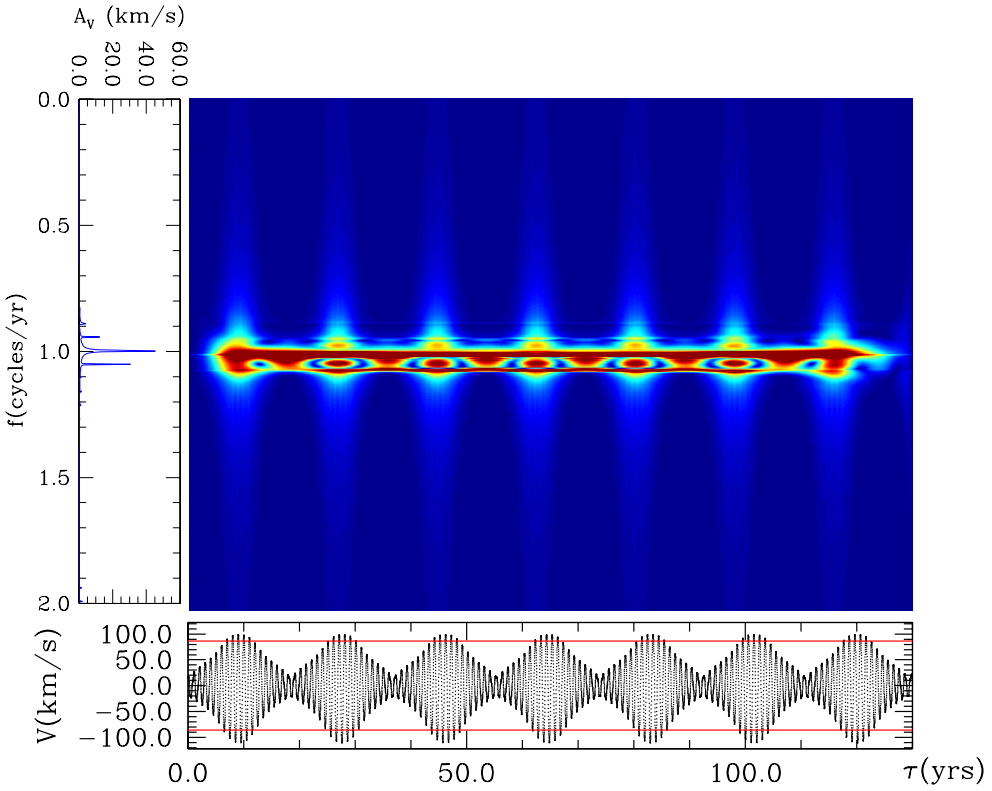

Figure 3.20: Choi-Williams distribution for the velocity variations of the case $\alpha = 0.3, \epsilon = 0.1902$, $(x_0, y_0) = (0.00, 0.25)$

(at least on the data they used). Regarding this last remark, further investigations carried out by the same authors (Buchler & Kolláth, 2001) led them to conclude that in general one cannot claim *a priori* that any of these methods is specifically superior to the others. In fact, this depends largely on the nature of the signal and on which kind of features one tries to enhance, and it is always therefore advantageous to use simultaneously several of them. However, as the Choi-Williams distribution is generally accepted to be the most useful among all the methods, we will center our analysis using this tool. For our calculations, we took σ=10, as it was done in Buchler & Kolláth (2001).

For illustrative purposes in the central panel of Figure 3.20 we show the Choi-Williams time-frequency analysis of the velocity variation for the case of $\alpha = 0.3, \epsilon = 0.1902$ and the initial condition $(x_0, y_0) = (1, 0.25)$. The bottom panel of Figure 3.20 shows the time series in order to better understand the Choi-Williams distribution, whereas the Fourier analysis is shown in the left panel. A close look at this last panel reveals beatings between two main frequencies. The period of the beatings is 8.81 years, as can be noticed approximately from this panel. Also, from the left panel of Figure 3.20 (which corresponds to the Fourier analysis) one can notice

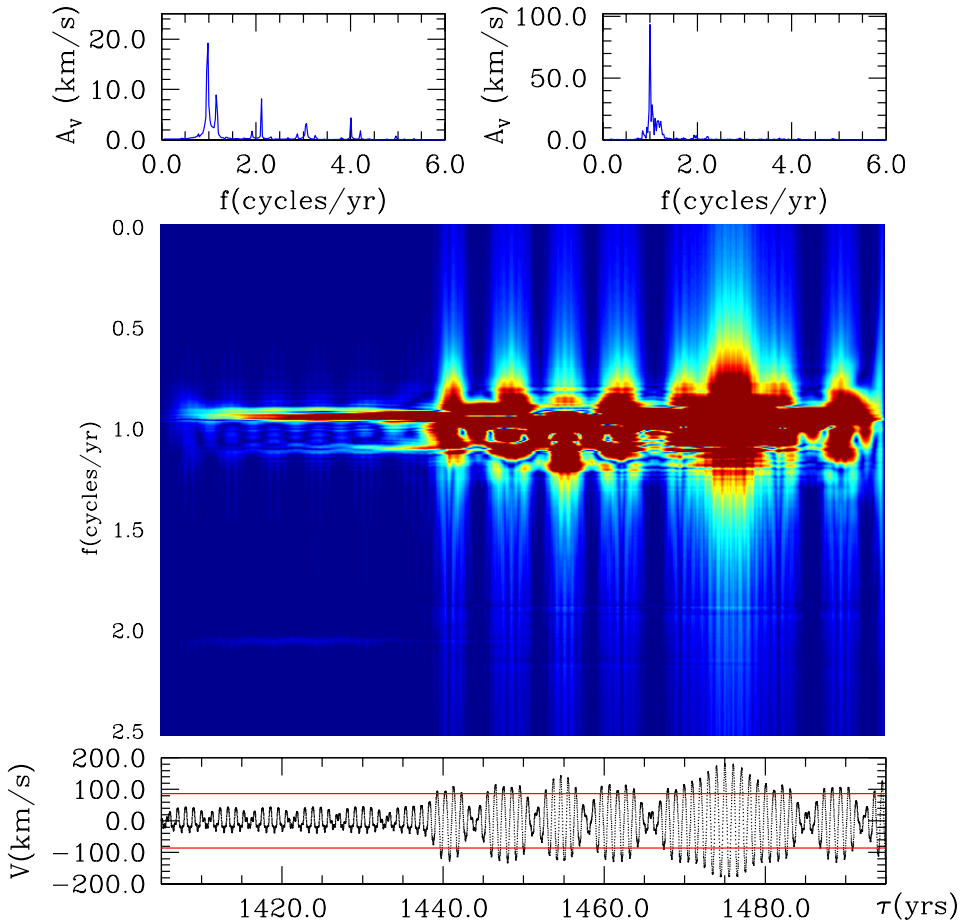

Figure 3.21: Choi-Williams distribution of the velocity variations for the case of Figure 3.17 *(central panel)*, Fourier analysis for $\tau < 1440$ yr *(top left panel)* and for $\tau \geq 1440$ yr *(top right panel)*, and the corresponding time series *(bottom panel)*.

clearly the presence of the beatings, since there are two main frequencies close one to another: the first at $f_1 = 1.0013$ yr^{-1} with $A_1 = 56.79$ km/s and the second at $f_2 = 1.0567$ yr^{-1} with $A_2 = 20.16$ km/s. Both frequencies can be clearly seen as well in the central panel of Figure 3.20, and the beatings are in this case most obvious, with a period of 18.05 yr. In this figure the escape velocity is represented as a horizontal line in the corresponding time series, and mass-loss is again very likely, since the velocity exceeds the escape velocity. The quasiperiodicity is easily noticed. Moreover, the amplitude modulation of the main frequency from the Fourier spectra is clearly visible in the time-frequency representation. Finally in this last case, the particular form of the envelope of the time-series results in an apparent spreading of the frequency, typical characteristic of a quasi-Dirac pulse.

Finally in Figure 3.21 the time-frequency analysis of the time series of Figure 3.16 is shown in the central panel. In order to be used as a visual help this time

series has been reproduced in the bottom panel of this figure. As we did in §3.3 with the Poincaré maps of this orbit, we have split the time series into two pieces, in order to better illustrate the stickiness of the oscillator, and we have computed the Fourier transforms of both pieces separately. These Fourier transforms are shown in the top panels of Figure 3.21, the left one corresponds to $\tau < 1400$ yr, whereas the right panel corresponds to $\tau \geq 1400$ yr. Note the difference in the scales of the power, which is much larger for the right panel. As it can be seen in these panels the power is suddenly shifted from larger frequencies to much smaller frequencies. This is even more clearly shown as well in the Choi-Williams distribution. Note as well the contribution of the frequency $f \simeq 2.1$ yr^{-1} at small times, just before the beginning of the burst (at $\tau \leq 1430$ yr). Indeed, this small contribution could be at the origin of the transfer of power to $f \simeq 1.2$ yr^{-1}, which occurs immediately after $\tau \simeq 1430$ yr and which ultimately leads to the burst at $\tau \simeq 1440$ yr. It is as well highly remarkable the small time elapsed since the beginning of the transfer of power, which is only about 10 yr.

3.5 Mathematic details of the dynamics

3.5.1 Comparison with the perturbed oscillator

In order to get a better insight of the dynamics of the oscillator studied so far, along this section we are going to compare it with the motion of a perturbed oscillator, which has been already studied extensively (Zaslavsky et al., 1991). This is important since, as it will be shown below the formal appearance of Eq.(3.6) does not differ very much from that of a perturbed oscillator. In order to make this clear consider the motion of a perturbed linear oscillator in the form of:

$$\ddot{x} + \omega_0^2 x = \epsilon \sin[\omega x - \omega t]. \tag{3.20}$$

The left-hand side of Eq.(3.20) describes very simple dynamics of linear oscillations of frequency ω_0. All the non-trivial types of motion arise from the perturbation one the right-hand side and its interaction with the unperturbed motion. To ease the comparison with the perturbed oscillator, Eq.(3.6) which describes our system, can be rewritten as:

$$\ddot{x} + \omega_0^2 x = -\epsilon[\omega x - \omega(t)t], \tag{3.21}$$

where

$$\omega(t) = \omega \left(\frac{b \sin \omega t}{t} + 1 \right). \tag{3.22}$$

As it can be seen both equations share common features. It is important to point out here that for our system $\omega_0 = 1$, as it results from Eq.(3.6). The explicit introduction of ω_0 in Eq.(3.20) will be used later to emphasize the importance of the

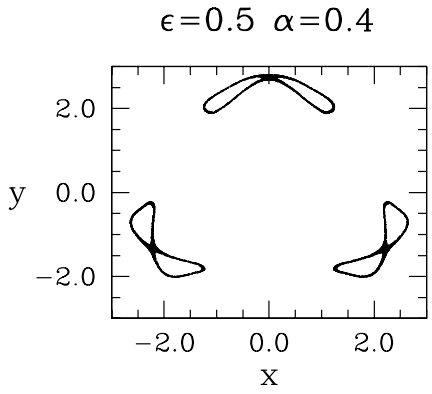

Figure 3.22: The period-3 homoclinic structure for $\alpha = 0.4$ and $\epsilon = 0.5$.

resonance condition, that is the case when the ratio $n \equiv \omega/\omega_0$ is a rational number. The hamiltonian associated with the system of Eq.(3.20) is:

$$H = \frac{(\dot{x}^2 + \omega_0^2 x^2)}{2} - \frac{\epsilon}{\omega}\cos[\omega x - \omega(t)t]. \tag{3.23}$$

Consequently, the results obtained so far and summarized in §3.2 (bifurcations and stochastic webs) should be similar to the case of a perturbed oscillator. And indeed this is the case, the only difference resides in the period 3 homoclinic orbit (see Figure 3.22), that is in point d) of the summary in §3.2. The creation of this period-3 homoclinic structure was illustrated in Figure 3.6 as α increases from $\alpha = 0.2$ to $\alpha = 0.3$. This suggests that the ultimate reason of this difference might be the presence of the function $\omega(t)$ from Eq.(3.22) as a weak detuning of resonance. In order to confirm this distinctive difference, we present in Figure 3.23 and Figure 3.24 the Poincaré maps for the following equations. First, we rewrite Eq.(3.21) — with $\alpha \neq 0$ — in the following way:

$$\ddot{x} + \omega_0^2 x = -\epsilon \sin\omega(x - t - b\sin\omega t)]. \tag{3.24}$$

Also we can set $\alpha = 0$ in Eq.(3.24) so we obtain:

$$\ddot{x} + \omega_0^2 x = -\epsilon \sin[\omega x - \omega t], \tag{3.25}$$

noticing that the difference between Eq.(3.25) and Eq.(3.20) resides only in the sign of the right-hand side.

As it can be seen in the previous equations, all three ODEs have the same mathematical structure. Due to the fact that the unperturbed equation ($\epsilon = 0$) is linear, the existence of the heteroclinic structures appears uniquely from the presence of the perturbation and they always transform to stochastic layers. It is generally called *"weak chaos"* — the perturbation itself creates the separatrix network at a certain ϵ_0 and then destroys it as ϵ increases beyond ϵ_0 by producing channels of chaotic dynamics (Zaslavsky et al. 1991). For the cases of *"strong chaos"*, the unperturbed hamiltonian H_0 intrinsically has separatrix structures and the perturbation clothes

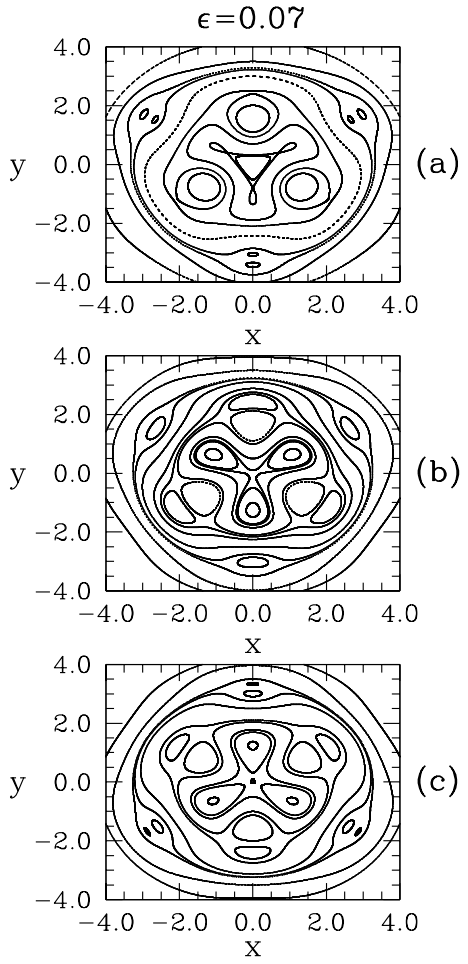

Figure 3.23: Poincaré map for Eq.(3.24), $\alpha = 0.3$ *(a)*, Eq.(3.25) *(b)* and Eq.(3.20) *(c)*. In all three cases $\epsilon = 0.07$.

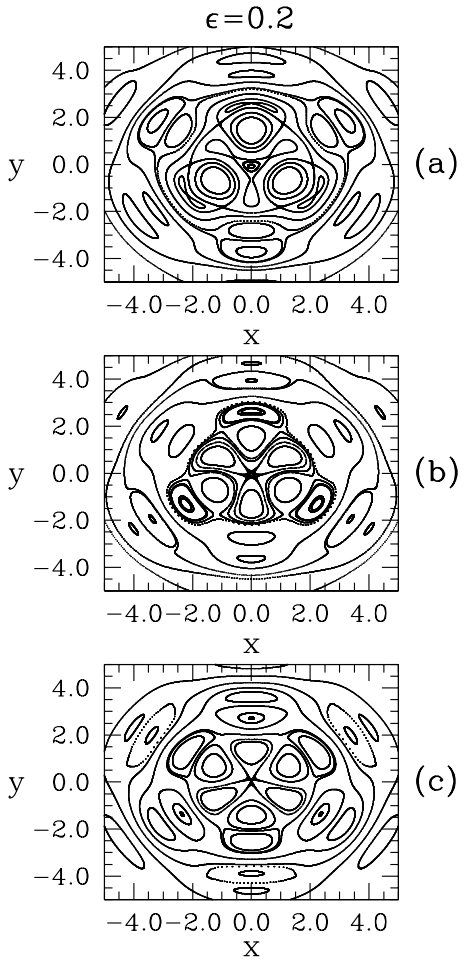

Figure 3.24: Poincaré map for Eq.(3.24), $\alpha = 0.3$ *(a)*, Eq.(3.25) *(b)* and Eq.(3.20) *(c)*. In all three cases $\epsilon = 0.2$.

them in thin stochastic layers. In fact, Figures 3.23 and 3.24 show better than the previous figures the symmetry due to the resonance as $n \equiv \omega/\omega_0 \approx 3$: rotational symmetry generated by $\omega_0^2 x$ with the angle $\theta = \pi/n$ as n is odd. In the phase space there appear invariant curves (deformed tori) embracing the center which do not allow diffusion in the radial direction. Inside these cells of the web, motion occurs along closed-orbits, around the elliptic points from the centers of the cells. With the increase of ϵ and creation of the stochastic layers, particles can wander along the channels of the newly born web, a phenomenon that represents a universal instability and gives birth to chaotic fluctuations. The heteroclinic structures formed as the perturbation increases through this bifurcation are what differentiates our equa-

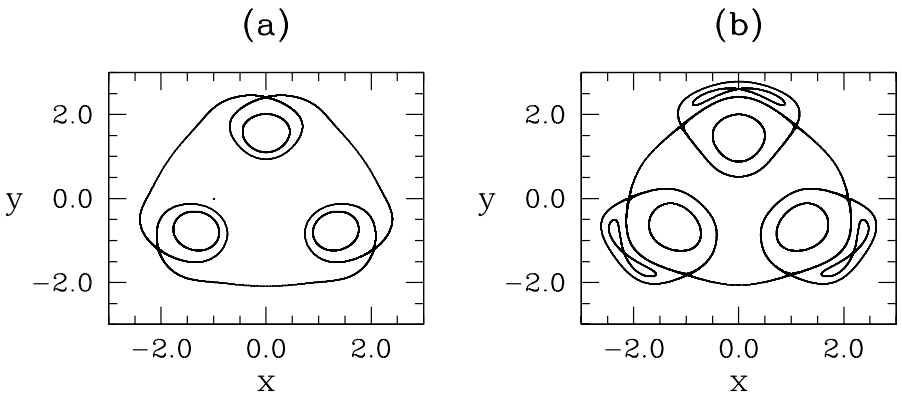

Figure 3.25: The distinctive separatrices for Eq.(3.24) differentiating its dynamics from that of Eq.(3.25): *(a)* $\alpha = 0.3, \epsilon = 0.07$ and *(b)* $\alpha = 0.3, \epsilon = 0.2$. For this case, only the period-3 homoclinic structure is the distinctive particularity. As ϵ increases the bifurcation is clearly seen.

tion from the typical equations of hamitonian chaos and in particular those of the perturbed oscillator. The bifurcation is better illustrated in Figure 3.25.

Before getting into the detailed analysis of the underlying cause of these bifurcations, we consider necessary to introduce the most important mathematical properties of the nontwist maps.

3.5.2 Typical features of nontwist maps

The general mathematical approach in studying area preserving maps (APMs) relies on the action-angle coordinates (r, θ) instead of the cartesian coordinates (x, y) — see Appendix A — with $x = \sqrt{2r}\cos\theta$ and $y = \sqrt{2r}\sin\theta$, and r is the momentum-like coordinate while θ is the angular variable. Under this coordinates and computing the angle without the restriction modulo 2π, one can associate to an orbit (r_n, θ_n) the rotation number which is the limit:

$$\rho = \lim_{n\to\infty} \frac{\theta_n - \theta_0}{2\pi n}, \tag{3.26}$$

if it exists. If ρ is an irrational number, then the orbit densely fills an invariant circle (i.e., a KAM circle), while an orbit of rational rotation number p/q — with p, q coprime integers, $q > 0$ — is a q–periodic orbit.

Typical questions of mathematical and physical interest include the persistence of the KAM circles after perturbation and determination of the threshold at which a circle of a given rotation number breaks up. The main results which answer these questions, such as the KAM theorem, the Poincaré–Birkhoff theorem, and the Moser twist theorem (Lieberman & Lichtenberg, 1992), are based on the validity of the twist property of the area preserving map transforming $(r, \theta) \mapsto (r', \theta')$, namely:

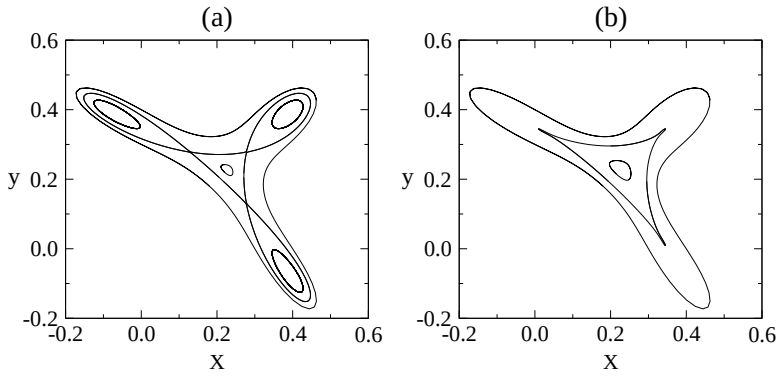

Figure 3.26: The triplication bifurcation in the cubic Hénon map. *(a)* The separatrix associated to the hyperbolic period–3 orbit of the map from Eq.(3.29), corresponding to $\mu = -1.13$, and some nearby orbits; *(b)* The same map at the saddle–center threshold $\mu_{\rm s} = -1.12189$. The twistless circle is the circle with three cusps.

$$\frac{\partial \theta'}{\partial r} \neq 0, \ \forall \ r \tag{3.27}$$

The twist condition implies the monotonic change of the rotation number ρ with r. The APM satisfying this condition is called monotonic twist map or simply a twist map.

Recently, due to the increasing number of physical phenomena that are modeled by nontwist maps, this class of dynamic systems has finally captured the attention of the scientific community. The prototype of nontwist APMs is the quadratic standard map (del Castillo Negrete et al., 1996; Petrisor, 2001):

$$\begin{aligned} r_{n+1} &= r_n - k \sin\theta \\ \theta_{n+1} &= \theta_n + 2\pi\omega - r_{n+1}^2 \ (\text{mod } 2\pi) \ . \end{aligned} \tag{3.28}$$

The twist condition is violated along the curve $r = k \sin\theta$. For $k = 0$ we get an integrable map, whose orbits lie on the circles of constant r. The rotation number function is $\rho(r) = \omega - r^2/(2\pi)$. The circle $r = 0$ has the maximum rotation number $\rho_{\max} = \omega$. It is called the twistless circle or shearless circle. A slight perturbation leads to the persistence of the twistless circle and nearby circles having a diophantine rotation number — that is, an irrational number badly approximated by rationals (Simó, 1998). Hence, the nontwist standard map, defined above, has an invariant circle of maximum rotation number among the rotation numbers of the nearby orbits.

There are many ways in which the monotonic twist condition can be violated. The vertical lines $\theta = \theta_0$ can be mapped into curves having a single extremum — quadratic twist (del Castillo Negrete et al., 1996) — or multiple extrema — cubic (del Castillo Negrete & Firpo, 2002), quartic (Howard & Humpherys, 1995) or sinusoidal twist (Saitou et al., 1997). Moreover, it has been proved (Dullin et al.,

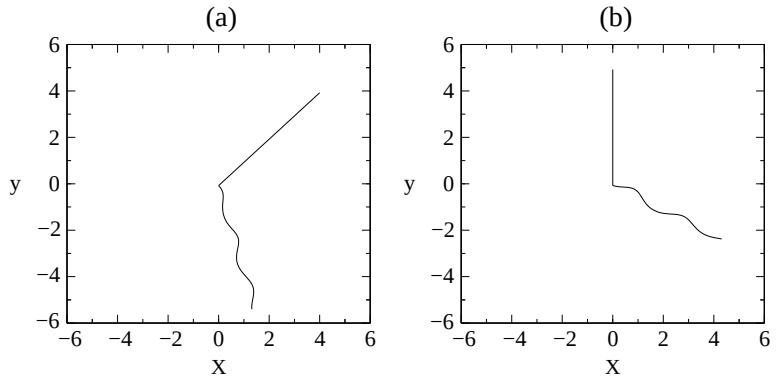

Figure 3.27: The nontwist property of the Poincaré map. *(a)* The effect of the map on the semi-line defined by $\theta = \pi/4$; *(b)* The effect of the map on the semi-line of $\theta = \pi/2$.

2000) that whenever the elliptic fixed point of an APM of the plane passes through a triplication, a twistless bifurcation occurs or, equivalently, the rotation number as a function of the distance from the elliptic fixed point becomes a nonmonotonic function. The triplication of the elliptic fixed point of an APM f_μ of the plane, occurs at the value $\mu \equiv \mu_3$ at which the multipliers of the elliptic point cross the values $\lambda = \exp(\pm 2\pi i/3)$. At the triplication threshold $\mu = \mu_3$ an unstable period–3 orbit emerges from the elliptic fixed point in both directions (see Figure 3.7), that is for $\mu < \mu_3$ and for $\mu > \mu_3$. As μ increases the elliptic point crosses the $1/3$ resonance and the triangular shape figure changes side after shrinking to an elliptic fixed point.

The typical case of triplication bifurcation is encountered in the dynamics of the cubic Hénon map

$$\begin{aligned} x_{n+1} &= -y_n + x_n^3 + \mu x_n + 0.7 \\ y_{n+1} &= x_n, \end{aligned} \tag{3.29}$$

which has an elliptic fixed point $(x_0, y_0 = x_0)$ that can be easily found. At $\mu_3 = -1.1505$ this point undergoes a triplication, while at $\mu_s = -1.12189$ the saddle center collision occurs. In Figure 3.26, we show that as μ increases beyond μ_3, the elliptic and hyperbolic period-3 orbits collide and disappear in a saddle–center bifurcation at $\mu = \mu_s$.

3.5.3 Generic and nongeneric properties of our Poincaré map

In the action-angle coordinates (r, θ) resulting from the change $x = \sqrt{2r}\cos\theta$ and $y = \sqrt{2r}\sin\theta$, the Hamiltonian of the system from Eq.(3.9) becomes

$$H(r,\theta) = r - \frac{\epsilon}{\omega}\,\cos(\omega\sqrt{2r}\cos\theta - \omega t - \alpha\omega^{1/3}\sin\omega t). \tag{3.30}$$

Due to the the complexity of the perturbative term of the Hamiltonian, the associated system is analytically intractable. In order to get some insight into its dynamic

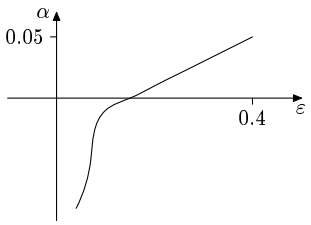

Figure 3.28: The curve $\alpha^*(\epsilon)$ whose points are the triplication thresholds of the central fixed point of the map P_ϵ.

behavior, we studied, as shown before, the Poincaré map (in fact the stroboscopic map) associated to this time-periodic Hamiltonian system. The unperturbed Hamiltonian $H_0(r,\theta) = r$ is globally degenerate, which means that $\partial^2 H_0/\partial r^2 = 0,\ \forall r$. The dynamic consequence of this degeneracy is that all the orbits are periodic having the same period. This is in contrast to KAM theory, where the unperturbed system is nondegenerate. We have seen that after a periodic perturbation (periodic in time and in space) the corresponding Poincaré map exhibits local and global bifurcations. In this section, we shall see that in some cases these are typical of the class of nontwist APMs, while in other cases are not.

The symmetry properties are very useful for the explanation of the behavior exhibited by the system under study. A system of differential equations can be written as

$$\dot{x} = F(x), x \in \mathbb{R}^n. \tag{3.31}$$

Since the Hamiltonian is time-periodic of period $T = 2\pi/\omega$, we define the function $s : \mathbb{R} \to \mathbb{S}^1$, $s(t) = t \pmod{2\pi/\omega}$, where $\mathbb{S}^1$ is the circle identified with the interval $[0, 2\pi/\omega)$, and then the system from Eq.(3.8) becomes the autonomous system of differential equations:

$$\begin{aligned} \dot{x} &= y \\ \dot{y} &= -x - \epsilon \sin(\omega x - \omega s - \alpha\omega^{1/3} \sin \omega s) \\ \dot{s} &= 1\,. \end{aligned} \tag{3.32}$$

We denote by Φ_t^ϵ its flow. Φ_t^ϵ associates to each triplet $(x_0, y_0, s_0) \in \mathbb{R} \times \mathbb{S}^1$ the position at the time moment t of the orbit starting at $t = 0$ from (x_0, y_0, s_0). The plane

$$\Sigma = \{(x, y, s) \in \mathbb{R}^2 \times \mathbb{S}^1 | s = 0\} \equiv \mathbb{R}^2 \tag{3.33}$$

is transversal to the flow and the map $P_\epsilon : \Sigma \to \Sigma$ defined by $P_\epsilon(x, y) = \Phi^\epsilon_{2\pi/\omega}(x, y, 0)$ is the associated Poincaré map.

The Poincaré map associated to the vector field F is reversible with respect to the involution $R : \Sigma \to \Sigma$, $R(x, y) = (-x, y)$ and therefore has the symmetry line

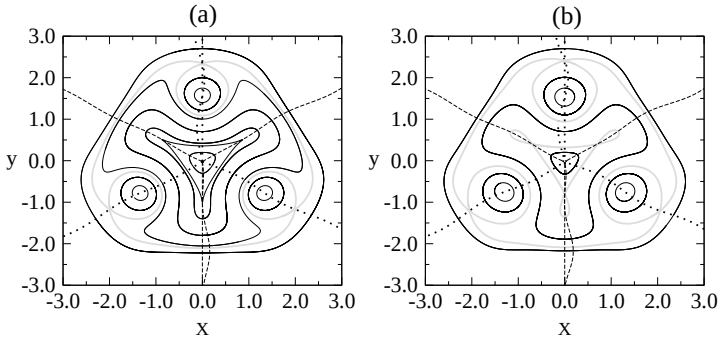

Figure 3.29: The Poincaré map P_ϵ before and after a saddle-center bifurcation. The figures display also the symmetry lines Γ^+_{2k} (dotted line) and Γ^-_{2k} (dashed line), with k=0, 1, 2, 3. *(a)* $\epsilon = 0.055$ — the phase portrait prior to the creation of the second dimerized island chain; *(b)* $\epsilon = 0.07$ — the second dimerized island chain has been created. The points satisfying $(x, y) \in \Gamma^\pm_0 \cap \Gamma^\pm_6$ are period–3 points.

$\Gamma_0 = \text{Fix}(R) = \{(x, y) \mid R(x, y) = (x, y)\}$, having the equation $x = 0$. Because the analytical expression for P_ϵ is not available, we cannot know the second reversor I from the usual decomposition of a reversible map as $P_\epsilon = I \circ R$. Hence the symmetry line $\Gamma_1 = \text{Fix}(I)$, as well as $\Gamma_{2k+1} = P^k_\epsilon(\Gamma_1)$ cannot be computed. We can however compute $P^k_\epsilon(\Gamma_0) = \Gamma_{2k}$.

The Poincaré map P_0 has the elliptic fixed point $(0, 0)$. After a slight perturbation the fixed point persists as a symmetric elliptic fixed point of the reversible map P_ϵ — it is a point $(0, y_\epsilon) \in \Gamma_0 \cap \Gamma_1$. In order to reveal the nontwist property of the map P_ϵ we compute and visualize the effect of the map on different semi-lines emanating from the elliptic fixed point (Figure 3.27). As it results from Eq.(3.26), the rotation number for the map P_0 is negative, more exactly $\rho = -1/\omega$. Unlike for the standard–like nontwist maps, here a line of constant θ is not mapped onto a parabola, that is a curve with a single extremum, but onto an oscillating curve, having many minima and maxima. This fact will lead to a different behavior of our nontwist map compared to the dynamic properties of nontwist standard–like mappings. More precisely, our map P_ϵ is a nontwist APM whose rotation number function $\rho(y)$ is oscillating, having more than one extremum, that is, more than one invariant circle whose rotation number is a local extremum — for more mathematical details, see also Munteanu et al. (2002).

We have shown in Figure 3.7 that for $\omega = 3.0146$, the Poincaré map P_ϵ associated to Eq.(3.32) has an elliptic fixed point which undergoes triplication. In Figure 3.28 we represent the triplication curve $\alpha^*(\epsilon)$. In the former figure, we illustrated the triplication bifurcation of the elliptic fixed point of the Poincaré map for $\epsilon = 0.07$ and $\alpha = -0.3$ — panel *(a)* — $\alpha = -0.05$ — panel *(b)* — and $\alpha = 0.02$ — panel *(c)*. We used values of α close to the ones from Icke et al. (1992) — $\langle\alpha\rangle \approx 0.3$ —

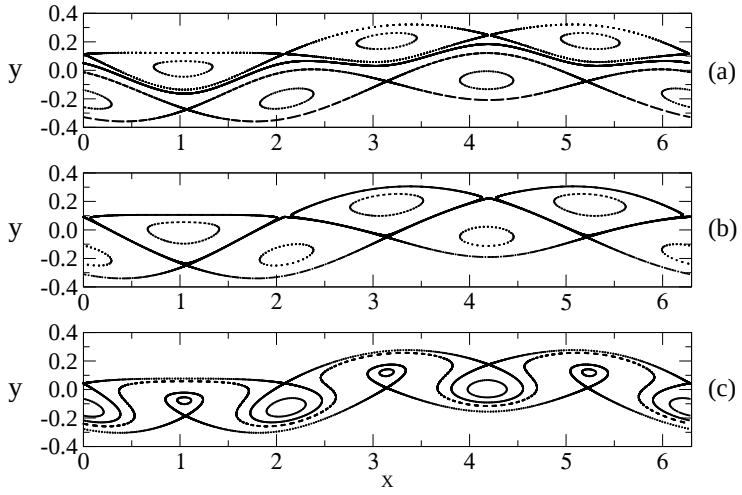

Figure 3.30: Reconnection process in the nontwist standard-like multi-harmonic map. *(a)* $\omega = 0.3287$ — two independent Poincaré-Birkhoff chains ; *(b)* $\omega = 0.3297655$ — the reconnection threshold; *(c)* $\omega = 0.3315$ — two dimerized island chains. We illustrate also a meander separating the two dimerized island chains.

in order to emphasize the role of ω and also to assure further comparison with their work. Thus, the considered pairs (ϵ, α) are located above the triplication curve.

We have shown in Figure 3.8 the separatrix structure called dimerized island chains. In order to show the successive births of period–3 orbits as ϵ increases with $\alpha = 0.3$ fixed, we compute and visualize $P_\epsilon^k(\Gamma_0^+)$ and $P_\epsilon^k(\Gamma_0^-)$, $k = 1, 2, 3$, with $\Gamma_0^+ = \{(x, y)|x = 0, y > 0\}$ and $\Gamma_0^- = \{(x, y)|x = 0, y < 0\}$. This process was first illustrated in Figure 3.27*b* where Γ_0^+ and $P_\epsilon^1(\Gamma_0^+) = \Gamma_2^+$ were represented. We show in Figure 3.29 the connection between the symmetry properties of the map and the creation of periodic orbits. A saddle-center bifurcation occurs at the value of the parameter ϵ at which $\Gamma_6^\pm$ has a tangential contact with $\Gamma_0^\pm$. The corresponding Poincaré map has for such an ϵ an invariant curve with cusps which represent the points of tangency. Increasing the perturbation, the two symmetry lines intersect at two points, one being elliptic and the other, hyperbolic.

A global bifurcation which is generic of nontwist maps is the so-called reconnection process, which is illustrated in Figure 3.30 for the nontwist multi-harmonic standard map (Petrisor, 2001):

$$x_{n+1} = x_n + 2\pi\omega + y_{n+1}^2 \pmod{2\pi} \tag{3.34}$$

$$y_{n+1} = y_n + k\sin[x_n + \arcsin(e\sin x_n)], \tag{3.35}$$

with $k = 0.2$, $e = 0.38$ and different values of ω. On the two sides of a twistless circle, two Poincaré–Birkhoff chains (necklaces of consecutive elliptic and hyperbolic

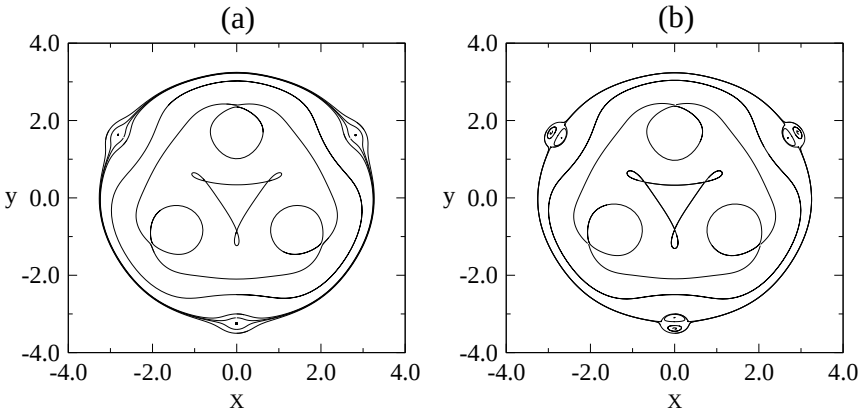

Figure 3.31: Creation of the first chain of vortices for $\alpha = 0.3$. *(a)* $\epsilon = 0.0614$ — the saddle-center bifurcation has created the first dimerized island chain; *(b)* $\epsilon = 0.06617$ — instead of a second dimerized island chain, a pair of vortices is born. See text for more details.

points), having the same rotation number, approach each other (Figure 3.30*a*). At a given threshold, which is called the reconnection threshold, their hyperbolic points are connected by heteroclinic arcs (Figure 3.30*b*). Varying the parameter of the system further, two dimerized island chains emerge from the configuration created by the reconnection (Figure 3.30*c*). These chains are separated by meanders.

In our case, we witness the creation of the nongeneric vortices or dipoles (del Castillo Negrete et al., 1996). Figure 3.31 displays the birth of the first chain of vortices. As ϵ increases, either Γ_6^+ or Γ_6^- intersects tangentially at a new point located at a radius larger than in the previous cases. As a consequence, new period–3 dimerized island chains are created after ϵ crosses the value of tangential contact. However, each second dimerized island chain has a different creation mechanism. Unlike the previous case, the hyperbolic point of the first dimerized island chain bifurcates into two hyperbolic points in the transversal direction. In this process, a new elliptic point is born on the symmetry line. These hyperbolic points are connected by three heteroclinic arcs: one surrounding the previously existing elliptic point, another surrounding the new elliptic point, and the third one separating the two elliptic points. Thus, a pair of vortices is created.

As ϵ increases, the process of formation of chains of vortices continues for larger radii (Figure 3.32). Note that if the elliptic orbits of one chain of vortices intersect Γ_0^+, then the next one, which is created external to it, has a pair of elliptic points on the symmetry line Γ_0^-. The invariant rotational circle interpolating the hyperbolic points of the chain of vortices is the twistless circle. In Figure 3.32 it can be seen that such circles pass almost through the extremum of the symmetry lines $\Gamma_6^\pm$. As already said, the formation of vortices is not generic and therefore the twistless circle that appears between them is not either.

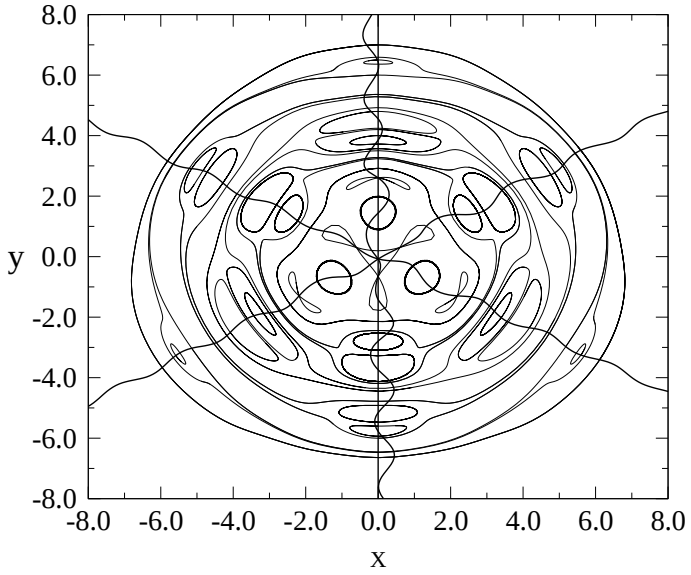

Figure 3.32: The phase portrait of the Poincaré map corresponding to $\epsilon = 0.2$ and $\alpha = 0.3$. One can see a sequence of concentric chains of vortices. The most exterior one is still incomplete. The figure displays also the symmetry lines $\Gamma^{\pm}_{2k}$, k=0, 1, 2, 3.

The existence of *meanders* was already mentioned in §3.2 (Figure 3.13). In twist standard–like maps they become usual invariant curves after the reconnection of the two chains. For the sake of clarity, we illustrate next the relationship between the meanders and the reconnection process for our map. In Figure 3.33 we show the creation of meanders from the reconnection of the Poincaré-Birkhoff chains of period 34. In the case of the standard nontwist map (del Castillo Negrete et al., 1996), in the reconnection of Poincaré-Birkhoff chains of even periodic orbits, fixed points of the chains having the same stability type are aligned in phase. In other words, to an elliptic (hyperbolic) point of one chain corresponds below or above also an elliptic (hyperbolic) point. Due to this alignment, the reconnection is nongeneric and corresponds to a hyperbolic-hyperbolic collision leading to the formation of vortices. In our case, the two Poincare-Birkhoff chains of even period (period 34) have fixed points of opposite stability type which approach each other in their way to reconnection (Figure 3.33*a*). Therefore, the reconnection is generic and in the subsequent dimerized islands chains, hyperbolic-elliptic collision occurs. Moreover, after the reconnection, the twistless circle turns from a graph of a function of the angular variable to a meander (Figure 3.33*b*). This meander is slightly visible in Figure 3.10*b*.

Meanders appear to be robust under the action of the perturbation, acting also as separatrices between distinct regions of chaotic dynamics. For stronger perturbations, their destruction allows the chaotic orbits to reach other stochastic regions pre-

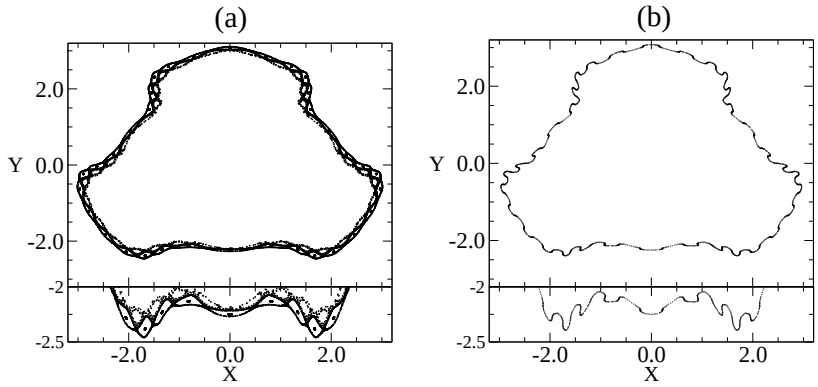

Figure 3.33: The reconnection process: *(a)* $\epsilon = 0.405$ — the Poincaré-Birkhoff chains confirming the generic process of reconnection illustrated in Figure 3.30; *(b)* $\epsilon = 0.4$ — after the reconnection, the resultant meander with 34 cusps, slightly visible in Figure 3.10*b*. At the bottom, the figures include a zoom for better view.

viously separated by the meander. This behavior was observed in nontwist standard-like maps (Simó 1998), but until now there is no explanation for this robustness.

3.6 Discussion

In this first part of our work, we have concentrated on the study of a forced oscillator which embodies the basics of the adiabatic stellar pulsations. We have extended this model to a range of values of the parameters specific to more massive and luminous stars than studied in a previous work. Compared to this previous work, our thorough parametric study of the extended model revealed a richer and more complex dynamics. In this sense, the model resulted to be of significant interest to us not only as a first step toward better modeling of stellar pulsations, but also as a mathematical object with distinctive properties. The latter aspect prompted us to undergo a comprehensive investigation on the mathematical causes of such a rich dynamics and the results have been extensively presented in the present chapter. Among the most significant results we mention the stickiness phenomenon characteristic of hamiltonian systems and the existence of sporadic episodes of mass loss resulting as consequence of the velocity of the outer layers exceeding the escape velocity.

Despite it being such a powerful trap to our mathematical interests with much more intriguing properties to discover, we have turned our attention to the physical aspects of the model. As discussed also in §1, an intrinsic variable star is one in which the nonadiabatic effects drive it to pulsational instability. Thus, the next step in our investigation centered on the importance of nonadiabaticity in simple models of stellar pulsations. This makes the object of the next chapter.

Chapter 4

Weakly nonadiabatic one-zone model

In Chapter 3, the equations of a simple approach describing the nonequilibrium mechanical behavior of a pulsating star have been analyzed and discussed. In essence, the model star was analog to a harmonic oscillator which was mathematically displaced from its equilibrium configuration and then released to begin its oscillations. As mentioned in §1.2, even if this adiabatic approach can account for some features of pulsating stars, it cannot provide information about what really causes the pulsations. Since energy transport was not considered, no information on the thermal behavior of the star and, therefore, on the most important observable, the light curve, was available. It also implies that the amplitude (whatever it may be) is forced to remain constant and thus it is not known what modes will grow and which will decay. In a nutshell, the equation describing the transfer of heat and radiation through the stellar environment must be incorporated, and this means that a nonadiabatic approach is compulsory. In the linearized nonadiabatic formulation (Eq. 1.14), we saw that the time-dependence of the pulsation characteristics was contained in (the real part of) $e^{i\sigma t}$, where σ was the complex frequency $\sigma = \omega + ik$. In this expression, ω is the usual pulsation frequency, while k is the stability coefficient leading to the definition of the growth or decay rate of the oscillations as $1/k$. In this Chapter, we shall consider thus the nonadiabatic extension of the model of Chapter 2. We shall introduce other one-zone models in addition to the ones from §1.5 and comment on their results. Next, we shall present our results and their comparison with observations, together with the mathematical description of the observed dynamic behavior.

4.1 An example of nonadiabatic one-zone model

Baker (1966) was the first to introduce the one-zone model as a tool to study the nonlinear behavior of stellar pulsations. As already mentioned in §2, Moore & Spiegel (1966) have also derived a self-excited nonlinear oscillator which relies on thermal dissipation for its excitation. In many senses it is, along with the Lorenz and Rössler systems (Strogatz 1994; Takeuti 1990), one of the classical low-order dynamic sys-

tems exhibiting rich chaotic dynamics (Balmforth & Craster 1997). Unfortunately, in contrast to the Lorenz and Rössler equations, it has received less serious attention. The work of Baker et al. (1971) delineated the conditions for the interesting aperiodic solutions found for this model. Buchler & Regev (1982) and Auvergne & Baglin (1985) later studied one-zone models under the assumption that the nonlinearity of the adiabatic coefficient Γ_1 is the main trigger for nonlinear pulsations through dynamic instability. Later on, Tanaka & Takeuti (1988) pointed out that dynamic stability might be necessary for realistic models of pulsating stars, which is the approach followed here.

In its simplest form, the study of stellar pulsations can be considered as a thermo-mechanical, coupled oscillator problem (Gautschy & Glatzel 1990). The coupling constant is given by the ratio of the dynamical to the thermal time scale in the outer layers of the star. Whenever the thermal time scale ($\tau_{\rm th} \sim 4\pi r^2 \rho \Delta r c_{\rm V} T / L_{\rm r}$) of an outer region of the star of radial extension Δr happens to become comparable to the sound-traveling time through that region ($\tau_{\rm dyn} \sim \Delta r / c_{\rm s}$), non-adiabatic effects are relevant. This implies that there is an efficient exchange of mechanical and thermal energies in that region. The ratio of the time scales is much smaller than one throughout most of the envelope and is close to unity only in the outermost regions. Significant non-adiabatic effects are relevant for helium stars, very massive AGB stars, some post-AGB stars and in the ionization zones of hot stars (Stellingwerf 1986; Gautschy & Saio 1995).

In order to derive the one-zone nonadiabatic model, we start by recalling the equation of motion and the energy equation without energy sources

$$\frac{d^2 R}{d\tau^2} = \frac{4\pi R^2}{m} P - \frac{GM}{R^2} \tag{4.1}$$

$$\frac{d \ln P}{d\tau} = \Gamma_1 \frac{d \ln \rho}{d\tau} - \frac{\chi_{\rm T}}{c_{\rm V} T} \frac{L - L_0}{m}, \tag{4.2}$$

where M is the stellar mass, L_0 is the luminosity at the base of the mantle, and R, P, T, ρ and L are, respectively, the radius, pressure, temperature, density and luminosity in the shell of mass m. In the present work, we will study the particular case in which L_0 is the (constant) equilibrium luminosity of the star, $L_\star$.

As introduced in §1.4, the κ- and γ-mechanisms provide the necessary driving for pulsations to occur and they reside in the layers of increased opacity. As a star oscillates, the location of the ionization regions changes both with respect to its radial position, r, and mass interior to r, $M_{\rm r}$. While this is certainly accounted for in a hydrodynamical approach of a multi-layered envelope, it is not straight-forward in a one-zone model where the derivatives with respect to r have been removed. A fit of this saturation of the κ-mechanism was introduced in a one-zone model approach by Saitou et al. (1989), the fit being a previous result of their multi-layered hydrodynamic models (Takeuti, M., private communication). It was introduced not only for evident physical reasons, but also to avoid divergence of the model and reach a

limit cycle. It is similar to the assumption of nonlinearity in the specific heat used by Buchler & Regev (1982). In their work, Eqs.(4.1-4.2) become

$$\begin{aligned} \frac{dr}{dt} &= v \\ \frac{dv}{dt} &= p\,r^2 - r^{-2} \\ \frac{dp}{dt} &= -3\Gamma_1 r^{-1} v p - \xi r^{-3}(r^{\beta} p^{\delta} - 1), \end{aligned} \tag{4.3}$$

where the variables r, v and p are the radius, velocity and pressure, respectively, expressed in nondimensional units as the radius and pressure were previously normalized to their equilibrium values. Additionally, the time t is expressed in units of the dynamic timescale (Eq. 1.1). The parameters

$$\beta = a(r^3 p - 1.2) + 21.6 \quad , \qquad \delta = 3.6 r^3 p (r^3 p - 0.2) \tag{4.4}$$

are the coefficients introduced by Saitou et al. (1989) as a saturation effect of the κ-mechanism with a being the control parameter. The nonadiabaticity parameter, ξ discussed in §2.5 is defined here as

$$\xi \equiv \left(\frac{GM}{R_\star^3}\right)^{-1/2} \frac{L_0}{m c_{\rm V} T_0}\,, \tag{4.5}$$

where the subscript 0 of the physical variables means the value in the equilibrium state. In their numerical analysis they use $\Gamma_1 = 5/3$ and $\xi = 0.08$ and show that the model becomes pulsationally unstable with the decrease of the control parameter a (decreasing temperature). The transition to the chaotic regime occurs through period-doubling bifurcations and accordingly, they recover the bifurcation diagram.

The behavior of any dynamic system $\dot{\boldsymbol{x}} = \boldsymbol{F}(\boldsymbol{x})$, with $\boldsymbol{x} = (x_1, x_2, ..., x_n)$ and $\boldsymbol{F} = (F_1, F_2, ..., F_n)$ is critically determined by its fixed points $\boldsymbol{x}_0$ given by $\boldsymbol{F}(\boldsymbol{x}_0) = 0$. The associated eigenvalues of the Jacobian matrix $(J_{\boldsymbol{x}_0})_{ij} = (\partial F_i/\partial x_j)_{\boldsymbol{x}_0}$ determine the nature of these fixed points. For instance, for a fixed point to be stable, it is required that all eigenvalues $\sigma \equiv \lambda \pm i\rho$ have negative real parts. In our case, the system has three fixed points: a trivial one, $(r_0, v_0, p_0) = (1, 0, 1)$ of mainly adiabatic origin with $\lambda \in \mathcal{R}_-$ and $\rho \in \mathcal{R}_+$, and two other fixed points, $(r_0^+, v_0^+, p_0^+) \approx (0.68, 0, 4.75)$ and $(r_0^-, v_0^-, p_0^-) \approx (8.8558, 0, 0002)$, entirely due to nonadiabatic effects (that is, they exist only for $\xi \neq 0$) and having $\lambda^+ \in \mathcal{R}_+$, $\rho^- \in \mathcal{R}_-$ and $\lambda_1^- \in \mathcal{R}_-$, $\lambda_{2,3}^- \approx 0$. For initial conditions close to the trivial fixed point, the period-doubling route to chaos was obtained by Saitou et al. (1989) by varying the control parameter a in the range $a \in [14, 20]$, while ξ was kept constant. However, no investigation on an equivalent effect produced by varying ξ was carried on. The Jacobian of the system calculated at the trivial fixed point has the form

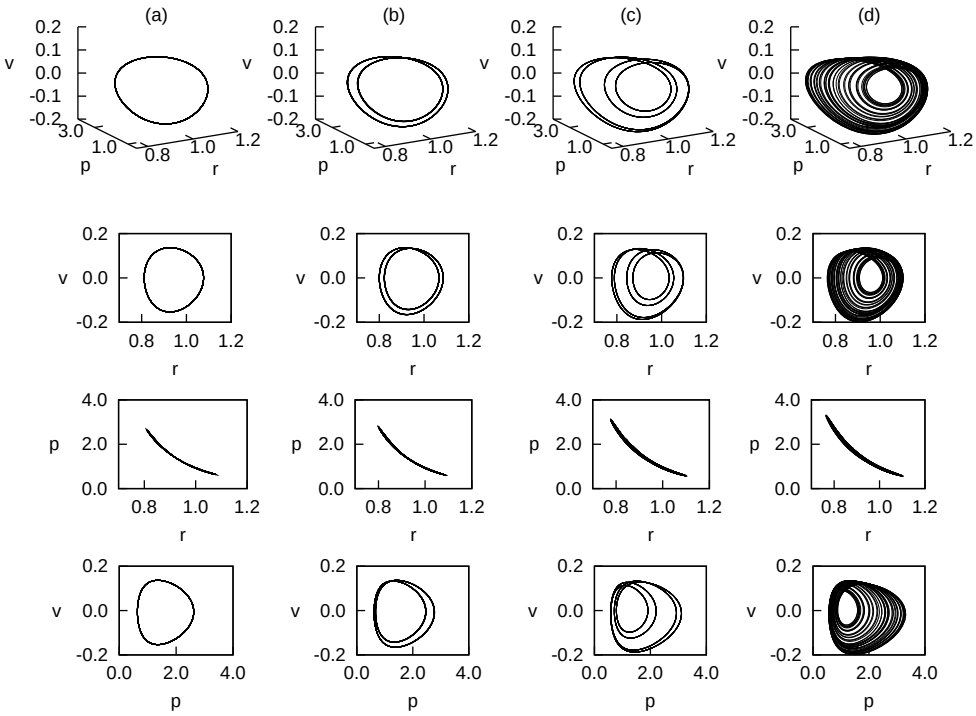

Figure 4.1: Period-doubling route to chaos represented in the space (r, v, p). In all panels, $\alpha = 0.1$, $\omega = 20.1$ and $a = 20$ have been adopted. *(a)* $\xi = 0.08$: Period-1; *(b)* $\xi = 0.09$: Period-2; *(c)* $\xi = 0.108$: Period-4; *(d)* $\xi = 0.12$: Chaos.

$$J_{(1,0,1)} = \begin{vmatrix} 0 & 1 & 0 \\ 4 & 0 & 1 \\ -\xi(21.6 - 0.2a) & -5 & -2.88\xi \end{vmatrix}. \tag{4.6}$$

The eigenvalues σ — and, therefore, the stability — depend on the parameters ξ and a. By solving the secular equation (i.e. $det|J_{(1,0,1)} - \sigma| = 0$) one can see that $\rho \geq 0$ for $a \leq 36$ and $\lambda \leq 0$ for $a \leq 50$, for any value of $\xi > 0$. As mentioned also by Saitou et al. (1989), the system is pulsationally stable for $a \leq 36$ and pulsationally unstable otherwise, for the initial conditions close to the trivial fixed point. A closer look to the roots of the secular equation shows that for $a \leq 36$, either the increase of ξ or the decrease of a leads to the same effect on the eigenvalues: $\lambda \in \mathcal{R}_-$ decreases while $\rho \in \mathcal{R}_+$ increases. The latter effect leads to chaotic behavior through the increase of pulsational instability. In favor of this statement and to complete their study, we present in Figure 4.1 a period-doubling route to chaos with the increase of the parameter ξ as it appears in the space (r, v, p).

4.2 Introducing the piston approximation

Next, we have concentrated our attention on the effects of the sub-photospheric piston on the model from Saitou et al. (1989). The piston approximation — first introduced by Bowen (1988) — used by Icke et al. (1992) is widely used in the literature (Fleischer et al. (1995); Höfner et al. (2003)). In general, time-dependent dynamic model atmospheres for AGB stars use a piston at their inner boundary (at $\approx 10^4 K$) and are based either on a grey atmosphere (Hoefner et al. 1998) or on a non-grey one (Höfner 1999). Even if it has never been scrutinized for validity, this approach appears to correctly reproduce the velocities and mass loss rates typical for AGB stars. Hence, this approximation can be regarded as a reasonable first-order approximation of the dynamic effect of the pulsation on the atmosphere.

In introducing the piston approximation for the one-zone model, we follow Icke et al. (1992) and Munteanu et al. (2002) in considering that the mechanical energy transmitted into the upper layers is proportional to the driving acceleration with a transmission coefficient Q defined by

$$A \;=\; -Q\,\frac{d^2 R_c}{d\tau^2}\,\Bigg|_{\rm ret} \tag{4.7}$$

and thus the final equations for our nonlinear nonadiabatic oscillator are

$$\begin{aligned}
\frac{dr}{dt} &= v \\
\frac{dv}{dt} &= p\,r^2 - r^{-2} - \\
&\quad -Q\alpha\omega^{4/3}\sin(\omega r - \omega t - \alpha\omega^{1/3}\sin\omega t) \\
\frac{dp}{dt} &= -3\Gamma_1 r^{-1} v p - \xi r^{-3}(r^{\beta}p^{\delta} - 1),
\end{aligned} \tag{4.8}$$

where the fractional amplitude, α and the characteristic frequency, ω are the parameters used in Chapter 3. The parameters that must be specified are Q, α, ω, Γ_1, a and ξ. We consider an ideal gas with an adiabatic coefficient $\Gamma_1 = 5/3$. For this study, we fix $\omega = 20.1$ ($R_0/R_\star$ is of the order of 15%) as the value adopted by Icke et al. (1992) for low-mass AGB stars, in order to pursue a further comparison of our nonadiabatic approach with their adiabatic one. We fix $a = 20$ as corresponding to the regular pulsation found by Saitou et al. (1989) and, moreover, we choose $\xi = 0.06$, a value close to the one used in their work. In our study, we have considered α and Q as main parameters in the control of the strength of the perturbation. As described in the following sections, our study revealed certain regions in the parametric space for which the model presents peculiar bursting oscillations. Its peculiarity and resemblance to some Mira light curves made us undergo a thorough investigation of this behavior and its dependence on the parameters. It lead us to conclude that, for a given ω, it is entirely characterized by the strength of the perturbation — by the

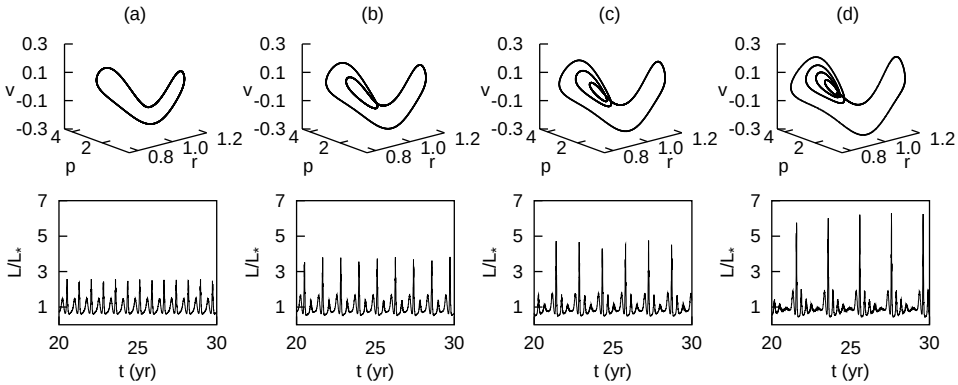

Figure 4.2: The birth of a knot-like structure for increasing values of Q. *Top panels:* Stroboscopic sampling of the orbit (r, v, p) with the characteristic frequency $\omega = 20.1$: *(a)* $Q = 1.02$, *(b)* $Q = 1.04$, *(c)* $Q = 1.08$ and *(d)* $Q = 1.16$. *Bottom panels:* The light curves corresponding to the cases shown in the upper panels.

pair (Q, α) — and not by the individual specific values of the parameters Q and α. In other words, given a fixed value of α, a certain range of values of Q can be found for which the same peculiar dynamics discussed below develop. First, we present the case of small internal perturbation ($\alpha \approx 3 - 4\%$) and amplified transmission through the envelope ($Q > 1$). Later on we will show that for higher (lower) values of the parameter α, the same behavior is encountered if lower (higher) values of the coupling coefficient Q are chosen. In addition, as the system from Eq. (4.8) presents a time-periodic perturbation, we shall use again the stroboscopic map in order to ease the visualization of the dynamics.

In the top panels of Figure 4.2 we present the stroboscopic map of the system for increasing values of Q. We notice the successive creation of loops, finally leading to a knot-like structure for strong perturbation ($Q = 1.16$). For the sake of comparison with real astronomical data, we also plot in the bottom panels of Figure 4.2 the nondimensional light curves for the corresponding cases. The luminosity L is obtained from the condition of radiative transfer together with the perfect gas law (see Eq. 2.44):

$$\frac{L}{L_\star} = r^\beta p^\delta, \tag{4.9}$$

where the normalizing constant $L_\star$ is the equilibrium stellar luminosity. The temporal scale is expressed in years and for this task we have used the stellar parameters associated to a typical Mira of $1\,M_\odot$ as they result from the work of Vassiliadis & Wood (1993).

The most striking feature of the light curves of Figure 4.2 consists in a highly energetic sporadic burst followed by a series of smaller peaks. A new peak appears with the creation of every new inward loop in the stroboscopic map. Each change in the number of loops is accompanied by a chaotic regime. The transition from a

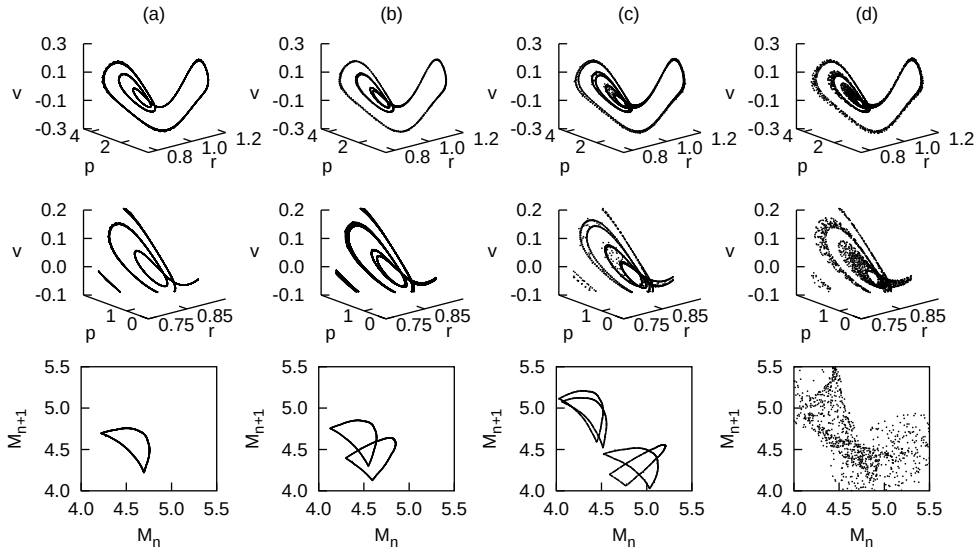

Figure 4.3: Transition to the chaotic bursting regime. *Top panels:* Stroboscopic map for the cases $\alpha = 0.037$, $\omega = 20.1$, $a = 20$, $\xi = 0.06$ and *(a)* $Q = 1.08$, *(b)* $Q = 1.07$, *(c)* $Q = 1.0615$ and *(d)* $Q = 1.055$. *Middle panels:* A zoom of the central loops of the stroboscopic maps of the top panel. *Bottom panels:* Return maps of the major peaks in the associated light curves.

regular regime, as in Figure 4.1, to a chaotic one occurs through a sequence of period-doubling bifurcations. In Figure 4.3 — upper and middle panels — we illustrate this behavior for values of the parameter $Q \in [1.06, 1.08]$. In the bottom panels of Figure 4.3 we present the return maps of the major bursts for the cases of the upper panels: plots of the maxima M_{n+1} versus the previous maxima M_n. This method appears to reveal with great clarity the period-doubling route to chaos, fact that justifies its application to this particular case.

For a clear exemplification of the chaotic regimes, in Figure 4.4 we show the light curves and the associated stroboscopic maps for a case of regular dynamics and for two cases of different degrees of irregularity. The central panels correspond to the case of regular dynamics prior to the development of the successive loops in the stroboscopic map. For a slightly lower value of the parameter Q (top panels), a completely irregular light curve results and the stroboscopic map clearly shows it. Finally, in the lower panels, we illustrate the dynamics of the system when Q takes a value corresponding to the accumulation of a sequence of period-doubling bifurcations.

Another important feature of the dynamics is the fact that the time interval $\tau_{\rm B}$ between major bursts increases with the strength of the perturbation, as it can be seen in the bottom panels of Figure 4.2. This is illustrated in Figure 4.5*a*, where the time interval between the successive major bursts is shown as a function of the cou-

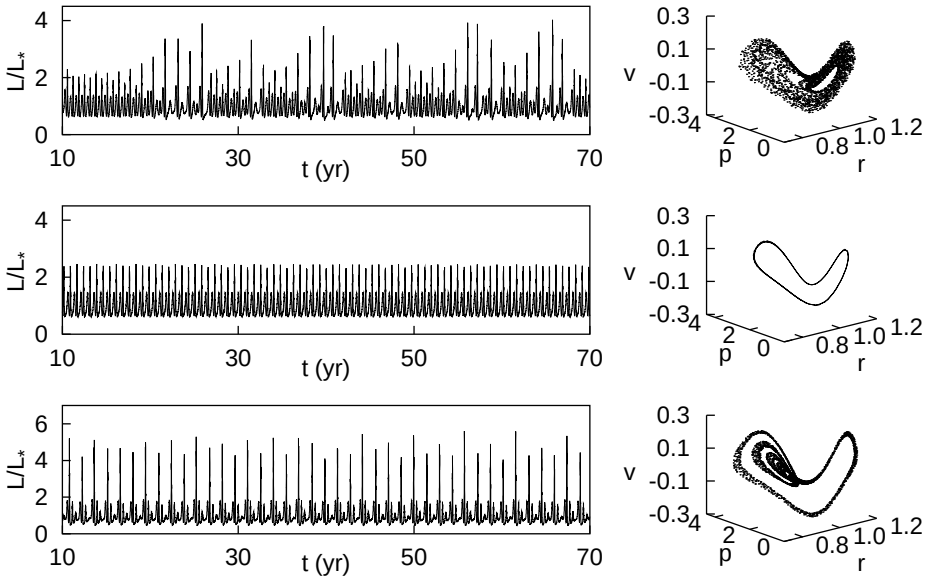

Figure 4.4: Comparison between regular and irregular dynamics. The light curves and the corresponding stroboscopic maps for the cases $\alpha = 0.037$, $\omega = 20.1$ and *(top panels)* $Q = 0.8$, *(middle panels)* $Q = 1.0$ and *(bottom panels)* $Q = 1.048$.

pling coefficient Q. As a visual guide we also plot the shape of the stroboscopic map at the fixed values of Q where an additional inner loop appears. As it can be seen in this panel and in panel 4.5*b*, $\tau_{\rm B}$ significantly increases for $Q \in [1.32, 1.39]$ whereas for $Q > 1.39$ (Figure 4.5*c*) the separation between successive bursts increases dramatically. Also, in Figure 4.5*b* we show that the above mentioned increase of $\tau_{\rm B}$ can also be obtained by decreasing the nonadiabaticity of the system (that is, decreasing ξ). Nevertheless the main parameter for tuning the time interval between major bursts turns out to be Q. Note as well that these major bursts favor mass loss at exceptionally high rates and, moreover, the time intervals between them are long. Hence, it is tantalizing to directly connect them with the periodicities observed in the circumstellar shells that can be found surrounding some planetary nebulae (Van Horn et al. 2003).

4.3 Mathematical interpretation of the results

In order to validate the numerical results discussed above, we briefly present the mathematical characteristics of our system. Given that our system is non-autonomous — that is, it is explicitly time-dependent — the typical methods of analysis of the theory of dynamic systems cannot be used. To overcome this drawback, we used an averaging method (Sanders & Verhulst 1985) to transform our system into an autonomous one. The high value of the characteristic frequency ($\omega \gg 1$) assures

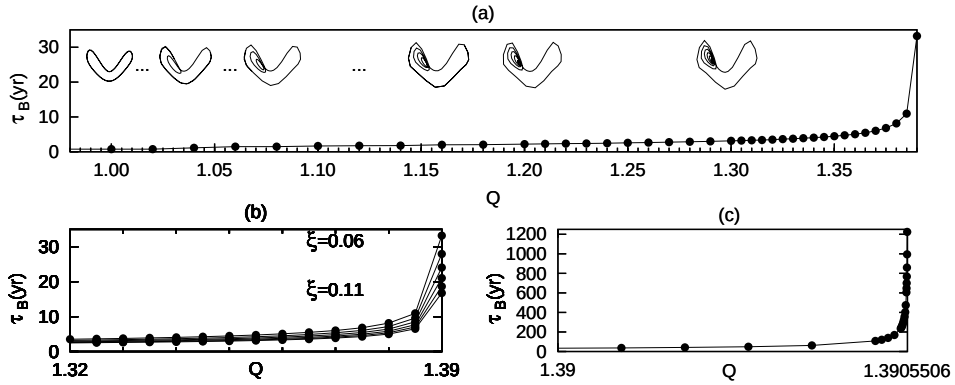

Figure 4.5: Time interval between bursting oscillations. In all cases, $\alpha = 0.037$, $\omega = 20.1$, $a = 20$. *(a)* Time between major peaks as a function of the strength coefficient Q for the case of $\xi = 0.06$; *(b)* Variation of the time between major peaks as a function of Q and for different values of ξ from 0.06 to 0.11; *(c)* The extension to higher values of Q leads to larger time intervals between major peaks for $\xi = 0.06$.

us that this method is applicable to our case. In the time-averaged framework, the time integral to be computed is

$$\begin{aligned} F(r) &= \frac{1}{T}\int_0^T \sin(\omega r - \omega t - \alpha\omega^{1/3}\sin\,\omega t)\,dt = \\ &= \sin\,\omega r\,\frac{1}{2\pi}\int_0^{2\pi}\cos(x + \alpha\omega^{1/3}\sin\,x)\,dx. \end{aligned} \tag{4.10}$$

Due to the particular complexity of this integral, we have resorted to numerical computation which led us into the following form of the averaged function:

$$F(r) = A\,\sin\,\omega r, \quad A = -0.04993. \tag{4.11}$$

In the time-averaged framework, the system from Eq.(4.8) becomes

$$\begin{aligned} \frac{dr}{dt} &= v \\ \frac{dv}{dt} &= p\,r^2 - r^{-2} - Q\alpha\omega^{4/3}F(r) \\ \frac{dp}{dt} &= -5r^{-1}vp - \xi r^{-3}(r^{\beta}p^{\delta} - 1). \end{aligned} \tag{4.12}$$

The fixed points of the system from Eq.(4.12) in the case of nonzero perturbation must satisfy the conditions:

$$p_0 = r_0^{-4} + Q\alpha\omega^{4/3}A\,r_0^{-2}\,\sin\,\omega r_0 \tag{4.13}$$

$$r_0^{\beta}p_0^{\delta} - 1 = 0\,. \tag{4.14}$$

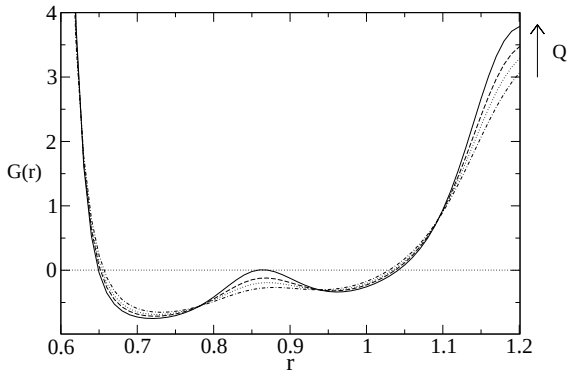

Figure 4.6: Numerical determination of the fixed points. The two fixed points $r_0 \approx 0.65$ and $r_0 \approx 1.03$ are inherited from the case of zero perturbation. The third new fixed point appears close to $r_0 \approx 0.85$ as Q increases at $Q \approx 1.3855$. The curves shown correspond to $Q = 0.8, 1.0, 1.16, 1.4$ (from bottom to top, as indicated by the arrow).

or, equivalently,

$$G(r) \equiv r^{\beta}(r^{-4} + Q\alpha\omega^{4/3}A \sin \omega r)^{\delta} - 1 = 0. \tag{4.15}$$

The roots of Eq. (4.15) are to be found again numerically. The behavior of this function in the range of interest $r \in [0.6, 1.2]$ is shown in Figure 4.6, where the horizontal line is used for a quick visual identification of the fixed points. The new fixed points $r_0 \approx 0.65$ and $r_0 \approx 1.03$ are only slight displacements of the fixed points mentioned before in the case of zero perturbation. Moreover, their associated eigenvalues maintain the form from the previous case. Increasing the parameter Q, a new fixed point is created at the central maximum of the function $G(r)$ at about $Q \approx 1.3855$. This new fixed point is stable as the associated eigenvalues have all negative real parts. With the creation of this fixed point, the looping behavior disappears. For higher values of Q, the fixed point is replaced by two unstable fixed points of saddle-focus type. The distance between them increases with $(Q - Q_0)^{1/2}$.

In order to verify both the applicability and robustness of the method, we studied the dynamics of the averaged system in search of the behavior observed in the non-autonomous system. The results appear in Figure 4.7 where the *trajectory in the phase space* (not the Poincaré map) of the averaged system for a selected range of parameters is shown. As it can be seen we obtain again the same interplay between the ejection loop and the inward spiraling, thus confirming the robustness of our simplified approach and the validity of results obtained for the non-autonomous system. In other words, we saw that the orbit sticks to a fixed point for a period of time that increases with Q.

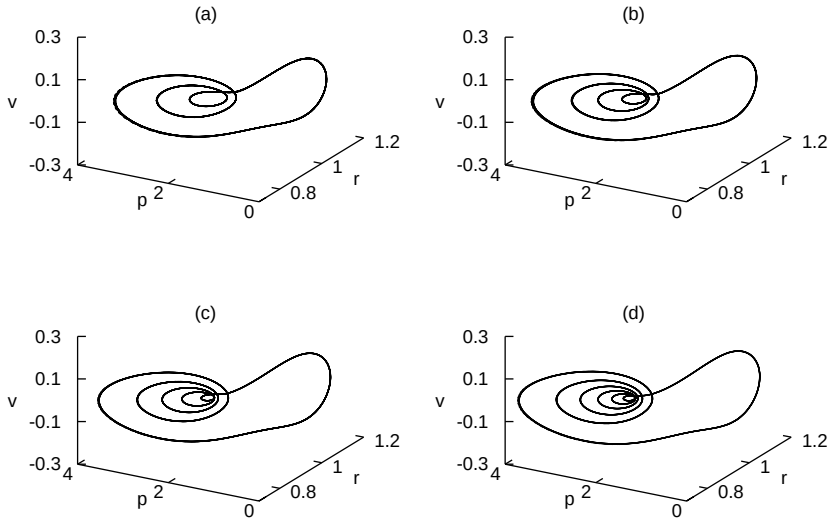

Figure 4.7: Phase space trajectory of the averaged system from Eq. (4.12). All the parameters are the same as in Figure 4.2 except: *(a)* $Q = 1.08$, *(b)* $Q = 1.14$, *(c)* $Q = 1.19$ and *(d)* $Q = 1.27$.

4.4 The role of ω

Before interpreting the behavior of the system in the context of real data of stellar variability, we consider worthy of interest the exploration of the role of the parameter ω and to justify the particular value we have used throughout this work. Icke et al. (1992) concluded that in the case of complete adiabaticity ($\xi = 0$), a decrease of ω leads to stronger chaotic pulsations. The values of ω used in their work were equivalent to adopting stellar models in the family of low-mass stars ($M \leq 8M_{\odot}$) reaching the AGB phase. In Chapter 3 — see also Munteanu et al. (2002) — we extended their conclusion to intermediate-mass stars ($8M_{\odot} \leq M \leq 11M_{\odot}$) also in the AGB phase, more precisely to values of ω around 3. In the previous sections, we have shown that in the case of $\omega = 20.1$ a peculiar behavior is born from the interplay between nonadiabaticity and internal perturbation. Our analysis of the system corresponding to the parametric interval $5 \leq \omega \leq 25$ has revealed that such a behavior is found for values of ω close to 20, that is for low-mass stars. Mathematically, we attribute this fact entirely to the creation of new fixed points mentioned in the previous section which critically alter the dynamics of the system. They exist for values of ω higher than about 18. For values slightly lower than 18, the dynamics resembles the one encountered for $\omega = 20.1$ (middle panels of Figure 4.8), but it does not present the successive creation of new loops. Instead, the change of the control parameter Q leads to a mixture of chaotic regimes and uncorrelated creation and disappearance of new loops. For completeness, we present in Figure 4.8 the light curves and the stroboscopic maps for three values of ω. For each case, the temporal scaling factor

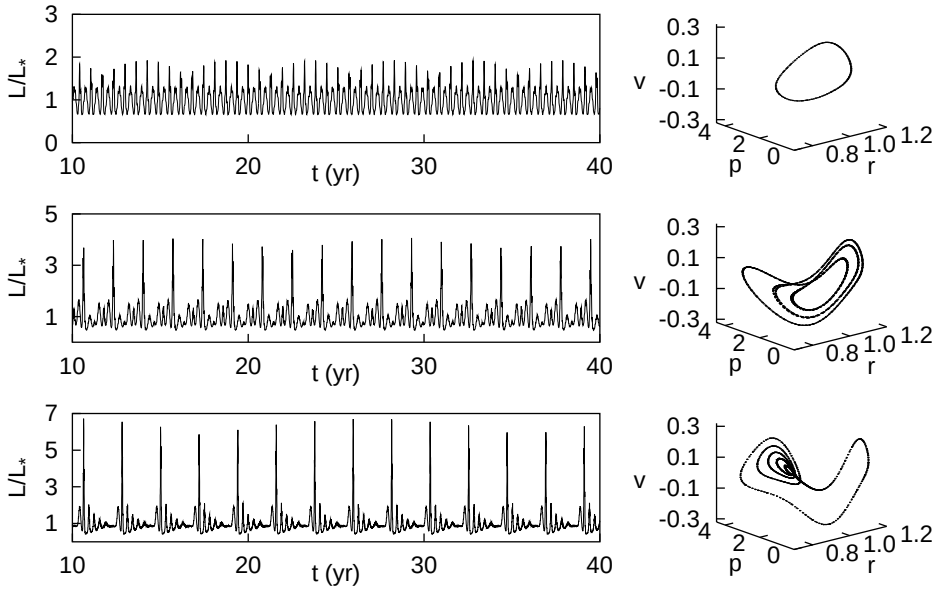

Figure 4.8: The role of ω. The light curves and the corresponding stroboscopic maps for the cases $\alpha = 0.037$, $Q = 1.2$ and *(top panels)* $\omega = 10$ ($M = 5M_{\odot}$), *(middle panels)* $\omega = 15$ ($M = 3M_{\odot}$) and *(bottom panels)* $\omega = 20.1$ ($M = 1M_{\odot}$).

was computed according to the work of Vassiliadis & Wood (1993) which provides a complete set of stellar parameters for AGB stars with initial masses in the range $0.89 \leq M/M_{\odot} \leq 5.0$. Due to the richness of the dynamics in the case of $\omega = 20.1$, we use it for a comparison with observations.

4.5 The strength of the perturbation

In §4.1 we anticipated the fact that the peculiar bursting regime described in the last sections was observed for certain values of the strength of the perturbation, that is for certain values of the pair (Q, α) and not for the individual specific values of the parameters Q and α. In this section we present the basis of this result.

The perturbation term considered in the case of the averaged system as depending only on the parameters Q and α can be extracted from Eqs. (4.12):

$$\mathcal{A}(\alpha, Q, \omega) = Q\alpha\omega^{4/3}\,\frac{1}{2\pi}\int_0^{2\pi}\cos(x + \alpha\omega^{1/3}\sin\,x)\,dx. \tag{4.16}$$

It suggests that for the case of constant ω, to any value of α there should correspond a series of values of Q for which the perturbation term equals the values associated to the creation of additional loops described in the last sections. To confirm this claim, we have varied α in the range $\alpha \in [0.03 - 0.1]$ searching for a behavior

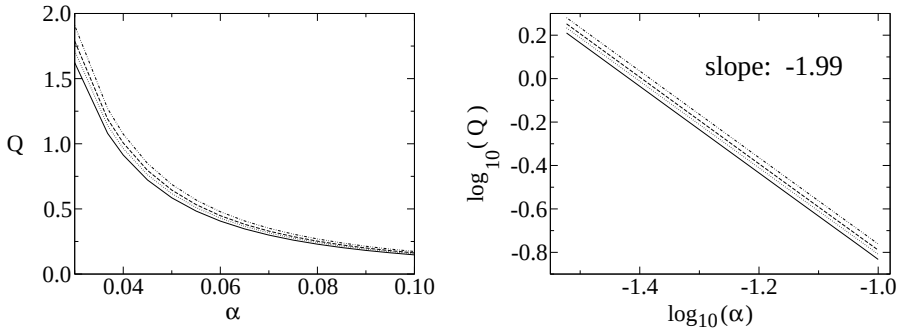

Figure 4.9: The curves (Q, α) corresponding to the formation of the $2^{\rm nd}$ (solid line), $3^{\rm rd}$ (dotted line), $4^{\rm th}$ (dashed line), and $5^{\rm th}$ loop (dot-dot-dashed line) for the averaged system from Eqs. (4.12).

similar to the bursting regimes described until now together with the successive creation of loops. We indeed identified the sequences of values of Q corresponding to the creation of the $2^{\rm nd}$, $3^{\rm rd}$, $4^{\rm th}$ and $5^{\rm th}$ loop as in Figure 4.7. In Figure 4.9*(a)* we represent Q as a function of α in the form of four curves traced by the values associated with the creation of the $2^{\rm nd}$, $3^{\rm rd}$, $4^{\rm th}$ and $5^{\rm th}$ loop. The log-log representation of the same data in Figure 4.9*(b)* illustrates a power-law dependence of the type $Q \sim \alpha^n$ with $n \approx -1.99$ to be at the root of the phenomenon. It is a reasonable approximation of Eq. (4.16) and therefore reflects the fact that the averaged perturbation term critically determines the dynamics.

4.6 Comparison with observations

The values of the parameters used throughout the numerical integrations were intended to locate the stellar models we are dealing within the family of Long Period Variables (LPVs) and, specifically, in the families of semiregular and Mira variables. The light curve of the prototype of the Mira stars, *o* Ceti, shows a peculiar variability consisting in an exceptional peak occurring every two, three or five "cycles" (Barthes & Mattei 1997). Our simple model naturally recovers this behavior by tuning the strength of the perturbation or the coupling coefficient. Moreover, we have shown that within our simple model large peaks in the light curve are associated to large interpulse intervals.

The Mira stars belonging to the Large Magellanic Cloud constitute the best sample of Miras concerning both periodicities and luminosities. In Figure 4.10*a* we show the observational data for some Mira stars in the LMC (Feast et al. 1989) and the best fit to the observational data. Among them, the ones having periods longer than about 400 days clearly appear to be over-luminous with respect to the period-luminosity relationship found for Miras with relatively short periods (Zijlstra et al. 1996; Bedding et al. 1998). With this in mind we have obtained a period-luminosity

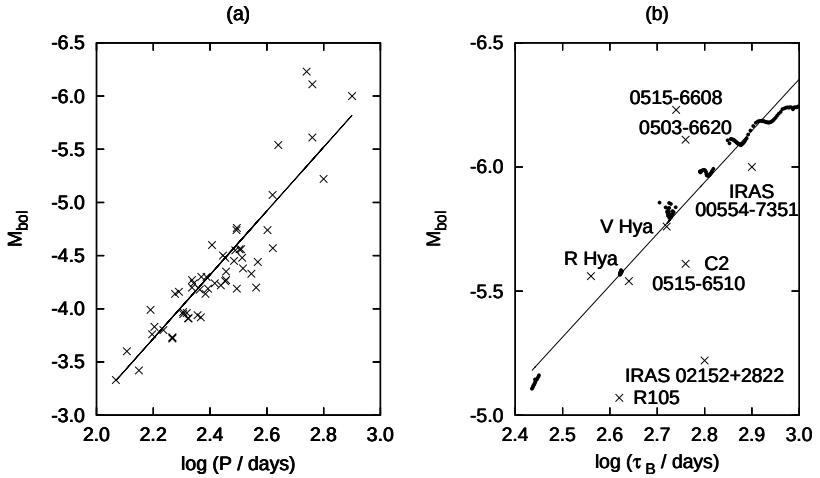

Figure 4.10: Period-Luminosity relation for Mira stars. *(a)* PL relation for Mira stars in the LMC and the data on which the relationship is based (Feast et al. 1989). *(b)* The PL relation using the data furnished by our model (filled circles): the equivalent $M_{\rm bol}$ of the major peaks and the time interval $\tau_{\rm B}$ between them. The values for the parameters used here are $\alpha = 0.037$, $\xi = 0.06$ and $Q \in [1, 1.26]$. The crosses represent a sample of over-luminous Mira stars in the LMC. See text for additional details.

relationship from our theoretical models using the time interval $\tau_{\rm B}$ and averaged values of the major peaks in luminosity. More precisely, we have varied the parameter Q in the range $[1, 1.26]$ resulting in light curves whose major peaks have periodicities (in days) within the range $2.4 \leq \log \tau_{\rm B} \leq 3.0$. The corresponding bolometric magnitudes were computed using a reference value for the equilibrium stellar luminosity of $L_\star = 10^{3.5} L_\odot$, which is typical for Mira stars. Our theoretical period-luminosity relationship is shown in Figure 4.10*b*. For the sake of comparison we also show in this panel all those Miras with $\log P > 2.4$ and $M_{\rm bol} < -5.0$, that is all the stars which are found to be over-luminous in Figure 4.10*a*. We have also included two other interesting Miras: R Hya and V Hya. As it can be seen our theoretical period-luminosity relationship fits very well the observational data. Moreover, note as well that the observations tend to cluster around fixed regions of the period-luminosity relationship. These regions are coincident with the regions where we find regular oscillations with a fixed number of loops in the stroboscopic map and its sequence of period-doubling cascade leading to chaos. The gaps between the theoretical data are the consequence of the drastic change in the characteristics of our light curves when a new loop is created, and correspond to a very small change of the coupling coefficient. Hence, according to our analysis we should not find almost any star in these regions, which is exactly what it is found.

Another peculiarity of Mira stars is that some of them show alternating deep and shallow minima, giving the appearance of double maxima. Some examples are

R Cen, R Nor, U CMi, RZ Cyg and RU Cyg — see Hawkins et al. (2001), and references therein. Among these, R Cen has the most persistent and stable double maxima in the light curve while for the rest of the cases the second maxima is often weak and the light curve sometimes reverts to that of a normal Mira. Our results provide such light curves for small values of the parameter Q. As for the general "chaotic connection" for the Mira variables, the first (and unique) case of evidence of chaotic pulsation in a Mira star (R Cyg) comes from the study by Kiss & Szatmáry (2002). They associate the long sub-segments of alternating maxima in R Cyg to a period-doubling event, supporting therefore the well-known scenario of period-doublings to chaos, which we also find in our model. Buchler et al. (2002) present an overview of observational examples of chaotic behavior in some semiregular variables (SX Her, R UMi, RS Cyg, and V CVn). They argue that AGB stars are prone to chaotic pulsations due to the fact that relative growth rates of the lowest frequency modes are of order unity. This condition is not fulfilled for the classical Cepheid variables that have growth rates of the order of a few percent and undergo periodic pulsations. Higher relative growth rates are a consequence of higher luminosity/mass ratio, that is more nonadiabatic stars. Hence, not only semiregular variables, but also Mira stars should also be candidates for chaotic pulsators. In spite of its simplicity, our one-zone model presents chaotic pulsations for certain intervals of the parameters characterizing the strength of the internal driving and, thus, could provide some support to the conjecture that the evolution of semiregulars and of Mira stars is strongly connected.

4.7 Discussion

In this second part of our study, we have concentrated our attention on the implications of nonadiabaticity in the context of simple models of stellar pulsations. Particularly, we have emphasized the consequences of the internal driving coupled with weak nonadiabaticity in the dynamic behavior of the upper stellar layers. As in the case of the previous chapter, we have encountered certain ranges of parameters leading to a peculiar behavior. It was characterized by bursting oscillations in the form of an energetic burst followed by a series of smaller peaks. Our results related this behavior strictly to the strength of the internal driving. Through the parametric study we followed the creation and disappearance of the bursting regime.

The nonadiabatic approach has allowed us the access to the most typical observable, the stellar luminosity. The values of the parameters used in the simulations corresponded to the class of Long Period Variables and thus the comparison with the observations was intended for this type of pulsating stars. Rewardingly, several peculiar Mira stars have resulted to present a bursting regime similar to the one encountered in our simulations. Moreover, the interval between the major peaks as a function of the strength of perturbation has reproduced with acceptable accuracy the period-luminosity of the Mira stars.

As mentioned in the Introduction, the pulsating stars of low effective temperature such as Mira stars are definitely characterized by extensive convective zones in the envelope. In spite of numerous works and models treating the pulsation-convection interaction, there is no consensus in the literature on the driving or quenching role of the convection on the pulsation. This makes the object of the next chapter.

Chapter 5

The convective one-zone model of Stellingwerf revisited

As discussed in §1, there is a series of narrow bands running across the HR diagram within which the ionization regions are located at such depths that the resultant driving is able to lead the star into pulsational instability. The two main bands correspond to: *a)* the ionization of hydrogen and neutral helium at low temperatures (e.g., Mira variables) and *b)* the ionization of hydrogen, neutral and once ionized helium for the classical instability strip (classical Cepheids). While the cut-off at high temperatures (the so-called "blue edge") appears to be due to the ionization region located too high in the atmosphere for it to be effective, the low-temperature cut-off (the "red edge") is more problematic. If the surface temperature of a star is too low, the onset of efficient convection in its outer layers may dampen the oscillations. As the transport of energy by convection is more efficient when the star is compressed, the convecting material may lose heat at minimum radius and cancel the effect of the ionization, thus quenching the pulsation. The red edge of the instability strip is generally thought to be the result of the damping effect of convection, but for giant stars like Miras, nonlinear effects (such as pulsation inducing mass loss) can be strong enough to produce significant departures from hydrostatic equilibrium and thus make the predictions of the location of the red edge even more uncertain. What is beyond any doubt is that the stellar structure in the upper part of the HR diagram shows, in the best of cases, weak convection zones, if not extended ones as in the case of Miras where convection must necessarily be included in the modeling of its dynamics.

The simplest model treating the interaction between pulsation and convection is the one of Stellingwerf (1986), a generalization of the one-zone model of Baker (1966). In this chapter, we present comments and caveats on the results obtained from this model as they appear in several papers in the literature, and we also introduce new results and further possible extensions of the model.

5.1 Caveats on the Stellingwerf model

The model studied here was derived using the radiative approximation of Stellingwerf (1972) — see §2.5 — and adding a simplified version of the convection formalism described in Stellingwerf (1982). For the radiative model briefly described in §2.5, we recall below the equation of motion (Eq.2.41) and the energy equation (Eq.2.45):

$$\frac{d^2X}{d\tau^2} = \beta(HX^{-(m\Gamma_1-2)} - X^{-2}) \tag{5.1}$$

$$\frac{dH}{d\tau} = -\xi X^{m(\Gamma_1-1)}[X^b H^{s+4} - L_{\rm i}/L_0], \tag{5.2}$$

where all the notations have been already described in §2.5.

Before getting into the details of the model, it is of certain importance to mention the differences between the two *normalizing schemes* used in several versions of the radiative one-zone model of Stellingwerf (1972). In Stellingwerf & Donohoe (1987), the time is normalized to the pulsation period instead of normalizing to the dynamical time scale. In this approach, the light curves are obtained by a process of double iteration: first, the shell thickness, that is the ratio $\eta = R_{\rm c}/R_\star$ between the core radius, $R_{\rm c}$ and the equilibrium radius, $R_\star$, is varied to obtain an oscillation period of unity. Then, the initial value of H, the nonadiabaticity variable, is varied to obtain periodicity. This is a method to produce periodic light curves for a model in which the pulsations are growing or decaying. In another approach of the same model (Stellingwerf et al. 1987), the time is taken in units of dynamical time scale. The nonadiabatic parameter, ζ, becomes

$$\zeta \equiv t_{\rm dyn}\,\frac{\rho_0(\Gamma_3-1)L_0}{P_0 m_{\rm S}}\ ,\ t_{\rm dyn} = \left(\frac{GM}{R_\star^3}\right)^{-1/2}. \tag{5.3}$$

with $m_{\rm S}$ being the mass of the shell, M and $R_\star$, the stellar mass and radius, respectively, and $t_{\rm dyn}$, the dynamical time. This method allows direct integration of the equations without the need of iterative improvement being, therefore, a more physical approach. It is also the method adopted in Stellingwerf (1986), as well as in §3 and §4. Within this approach, the resultant time-series may be periodic or aperiodic as the shell may exhibit either a limit cycle or damped/growing oscillations.

The *damping* of the internal radiative regions of the star is generally not included in one-zone models. The one-zone model of Stellingwerf considers a form of damping produced by the radiative layers deeper than the pulsating shell. The functional form of the damping is reflected in the interior luminosity as it is allowed to vary with respect to the equilibrium luminosity as $L_{\rm i}/L_0 = X^u$, where the parameter u is normally negative as these layers damp the pulsation. In Stellingwerf & Donohoe (1987), the exponent u is given by

$$u = m[(s+4)(\Gamma_1 - 1)] - 4 \approx 7, \tag{5.4}$$

where the values for m, the parameters of the κ-mechanism s and n, and Γ_1 refer to the interior, not to the shell as in the calculation of the exponent b for the radius component of the outer luminosity, $L/L_0 = X^b h^{s+4}$. However, even if it is obvious that in this work the u-exponent is taken as having the same form as b (see Eq.2.46) from the usual diffusion formula for the luminosity, multiplied by -1 to account for a damping behavior, no argumentation for this approach is given. In general, the value $u = -2$ is arbitrarily adopted in most of the previously mentioned papers where the internal damping is considered.

The pulsational stability condition in the radiative case: $b - u < 0$ indicates that the only parameters affecting the driving or damping in the pulsating shell are the radius exponents of the luminosities (internal, u, and superficial, b). However, the introduction of the damping as described above does not lead to a more stable dynamics, as the role of damping should be. On the contrary, this functional form enhances the driving in the shell. This statement appears obvious directly from the pulsational stability condition, $b - u < 0$, where the addition of the negative factor u makes it more difficult to be fulfilled. Moreover, our calculations confirmed the increase of pulsational instability with the introduction of this damping term. It is worth adding also that in the above-mentioned paper the calculations involve an *ad hoc* choice of m, a guess for u, and a couple of tries for the initial radius, X_0 to obtain reasonable luminosity amplitudes. Additionally, in the same paper, it is mentioned that, for the convective case, the values of the parameters chosen to exemplify the blue-strip-red models for Cepheids are essentially arbitrary and are not based on detailed models. In this chapter we shall explore the connection between the values of the parameters and the physics expected from the model. Only such values can provide a useful comparison with the observational data and can be trusted to give a valid calibration of evolutionary models, too.

5.2 Coupled convection and pulsation

In Stellingwerf (1986), the nonlinear, nonlocal, time-dependent treatment of convection introduced in Stellingwerf (1982) is applied to the one-zone model leading to a simple convection scheme which has as limiting cases the "frozen-in" convection and the "mixing-length" convection. The root-mean-square convective velocity, U' obeys a "phase lag" equation of the form

$$\frac{\partial U'}{\partial \tau} = \zeta_c (U_{\rm ml} - U'), \tag{5.5}$$

where $U_{\rm ml}$ is a mixing-length convective velocity and ζ_c is the convective efficiency defined as the ratio between the dynamical time scale and the convective adjustment time scale. The definition of the convective time scale is considered as one of the

main problems and it appears under question mark in Stellingwerf (1986), attracting our attention for further studies.

By using Eq.(5.5) together with Eqs.(5.1) and (5.2), and adapting them to a normalization scheme in which the dynamical time scale is used, the final equations describing the dynamics are obtained:

$$\frac{d^2X}{d\tau^2} = HX^{-q} - X^{-2} \tag{5.6}$$

$$\frac{dH}{d\tau} = \zeta X^{2d}(1 - \gamma_r X^b H^{s+4} - \gamma_c X^{-c} U_c^3) \tag{5.7}$$

$$\frac{dU_{\rm c}}{d\tau} = \zeta_{\rm c}(X^{-d}H^{1/2} - U_{\rm c}), \tag{5.8}$$

where $U_{\rm c} \equiv U'/U_{\rm ml_0}$, $q \equiv m\Gamma_1 - 2$, $d \equiv m(\Gamma_1 - 2)/2$ and $c \equiv m - 2$, while the other quantities have the meanings described in §2.5. The convective/radiative splitting is given by the parameter $\gamma_{\rm c}$ defined by the ratio between the initial convective luminosity and the total initial luminosity, that is $\gamma_{\rm c} \equiv L_{\rm c_0}/L_0$. Thus, the parameter $\gamma_{\rm r}$ is $\gamma_{\rm r} = 1 - \gamma_{\rm c}$. In order to determine the stability properties of the above system of differential equations, one has to linearize the equations about the equilibrium fixed point $(\bar{X}, \bar{V}, \bar{H}, \bar{U_c}) = (1, 0, 1, 1)$ through the change of variables $X = 1 + xe^{\sigma t}$, $H = 1 + he^{\sigma t}$, $U_{\rm c} = 1 + u_{\rm c}e^{\sigma t}$ and further construct the secular equation of the eigenvalues σ which results to be of the type

$$A + B\sigma + C\sigma^2 + D\sigma^3 + \sigma^4 = 0, \tag{5.9}$$

where

$$A = \zeta\zeta_{\rm c}[P + RQ + 3\gamma_{\rm c}(R/2 - d)], \tag{5.10}$$

$$B = \zeta_{\rm c}R + \zeta(P + RQ), \tag{5.11}$$

$$C = \zeta\zeta_{\rm c}(Q + 1.5\gamma_{\rm c}) + R, \tag{5.12}$$

$$D = \zeta_{\rm c} + \zeta Q, \tag{5.13}$$

with $P \equiv \gamma_{\rm r}b - \gamma_{\rm c}c$, $Q \equiv \gamma_{\rm r}(s + 4)$ and $R \equiv q - 2$. The complete stability of the system is assured if all the eigenvalues (the roots of Eq.5.9) have real part, which according to Stellingwerf (1986) leads to:

$$\text{Turbulent stability}: \quad A > 0, \tag{5.14}$$

$$\text{Secular stability}: \quad B > 0, \tag{5.15}$$

$$\text{Dynamic stability}: \quad BC - AD > 0, \tag{5.16}$$

$$\text{Pulsational stability}: \quad D(BC - AD) - B^2 > 0. \tag{5.17}$$

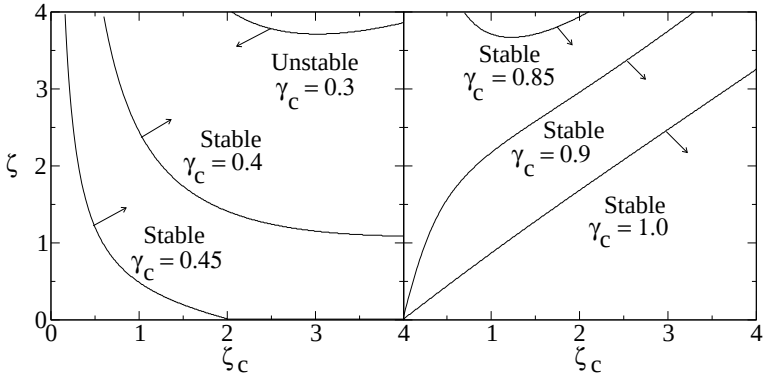

Figure 5.1: Location of pulsationally stable and unstable regions in the (ζ, ζ_c) plane for various values of γ_c, as obtained in Stellingwerf (1986).

While the values $n = 1$ and $s = 3$ for the parameters of the Kramers law are standard values, the ones of Γ_1, m, γ_c, ζ and ζ_c must be considered with caution. The value of $\Gamma_1 = 1.1$ adopted in Stellingwerf (1986) is a typical minimum one as the γ-mechanism operating in the ionization regions produces values of Γ_1 lower than 4/3. The value of m is quite crucial for the dynamics as Eq.(5.14) predicts instability if the shell is too thick (i.e., requires $m > 8$ for $\gamma_c = 1$). The choice of $m = 10$ of Stellingwerf (1986) together with the values already mentioned for the others parameters assure the turbulent stability as well as the dynamical and secular stability for ζ and ζ_c in the range $[0, 10]$ and $\gamma_c \leq 1$. On the other hand, Eq.(5.17) leads to both stability and instability for the ranges of interest. As also presented in Stellingwerf (1986), the location of the pulsationally stable and unstable regions in the (ζ, ζ_c) plane for various values of γ_c are shown in Figure 5.1.

In Stellingwerf (1986) a comparative study was done concerning what were considered to be models of pulsating stars in the vicinity of the Cepheid instability strip, more precisely the blue, the strip and the red cases. The values of the parameters chosen essentially arbitrarily happened to lead to the "blue" and the "strip" cases being pulsationally unstable (growing amplitude) and the "red" case, stable (decaying amplitude). Due to the arbitrary nature of the values of the parameters and to the absence of a limit cycle for these cases, the discussion of the time variations of the variables during a couple of quasi-periods is questionable in terms of the relevance of any possible conclusion regarding the form of the time series. A certain relevance could be attributed to the time series only in the case of existence of a limit cycle, in the context of a large range of γ_c, ζ and ζ_c. The linear stability analysis done in Stellingwerf (1986) was presented as leading to nonperiodic curves showing either damped (all eigenvalues have negative real parts) or growing oscillations (at least one eigenvalue has positive real part). While this interpretation is perfectly valid in the case of real eigenvalues, it may not be completely true if some eigenvalues are complex, as in this case certain bifurcations may occur in which periodic orbits (limit cycles) are born. Our calculations have revealed that indeed there are regions in the

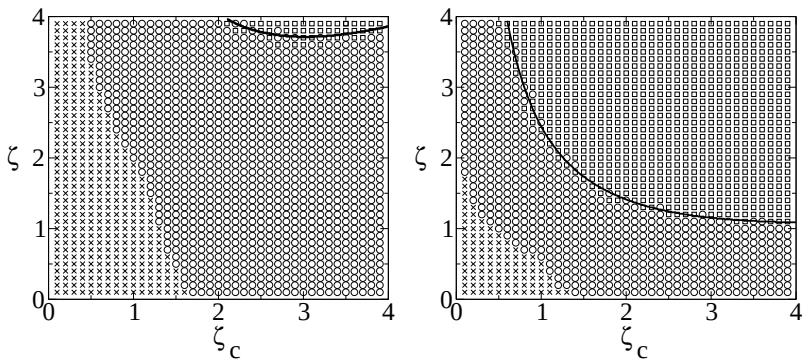

Figure 5.2: Location of the limit cycle regions (circles) as well as pulsationally stable (squares) and unstable regions (stars) in the (ζ, ζ_c) plane for $(X_0, V_0, H_0, U_{c_0}) = (1.4, 0.0, 1.0, 0.7)$ and *(a)* $\gamma_c = 0.3$ and *(b)* $\gamma_c = 0.4$. The black lines represent the lines of linear stability from Figure 5.1.

(ζ, ζ_c) plane where limit cycles exist for various values of γ_c. In Figure 5.2 we show the cases of $\gamma_c = 0.3$ and $\gamma_c = 0.4$ represented in the spirit of Figure 5.1. We show as white circles the cases in the plane for which limit cycles exist. For the numerical analysis, we have used the embedded 8^{th} order Runge-Kutta Prince-Dormand method from the GNU Scientific Library and adopted a tolerance of 10^{-10}. A limit cycle was considered to have been reached when consecutive maxima of the radius differed by less than 10^{-7}. A damping solution was considered when the solution was tending asymptotically to the fixed point $(\bar{X}, \bar{V}, \bar{H}, \bar{U}_c) = (1, 0, 1, 1)$ and the distance to it was less than 10^{-8}. For values of the radius greater than $X = 15$, the solution was considered unstable.

The typical bifurcation responsible for the creation of limit cycles is the Hopf bifurcation (Strogatz 1994). There are two types of Hopf bifurcation generally known as the *supercritical* and the *subcritical*. The former is the one that characterizes the behavior of Eqs. (5.6–5.8) and therefore will be discussed below. If some of the eigenvalues of the linearized system are complex, then it is possible that, by continuously changing the values of the parameters, the real part of a pair of complex eigenvalues crosses the imaginary axis from the negative domain to the positive domain giving birth to a limit cycle. In order to exemplify the dynamics, let us consider the case of $\gamma_c = 0.4$. For values of the parameters ζ and ζ_c from the green region in Figure 5.2*b*, all eigenvalues have negative real part ($\text{Re}(\sigma) < 0$) and thus the equilibrium point $(\bar{X}, \bar{V}, \bar{H}, \bar{U}_c) = (1, 0, 1, 1)$ is stable (i.e. stable focus). This is the case of damping oscillations found in Stellingwerf (1986). For all the values of the parameters from Figure 5.2*b*, the linearized system presents one pair of complex eigenvalues whose real part becomes positive when the pulsational stability condition is broken. After the bifurcation point characterized by $\text{Re}(\sigma_\pm) = 0$, where $\sigma_\pm$ is the pair of complex eigenvalues, the equilibrium point has become linearly unstable and a stable closed orbit is surrounding it. A schematic view of this bifurcation appears in Figure 5.3.

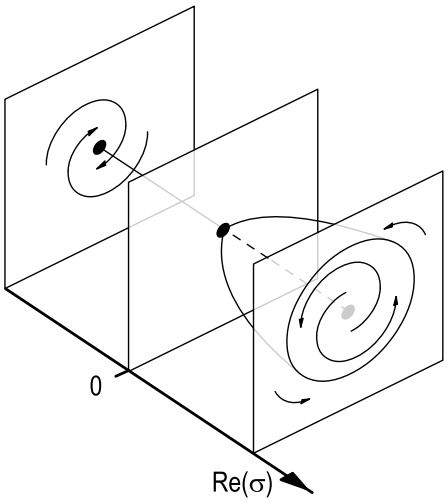

Figure 5.3: The supercritical Hopf bifurcation in a 2D system and the birth of a limit cycle.

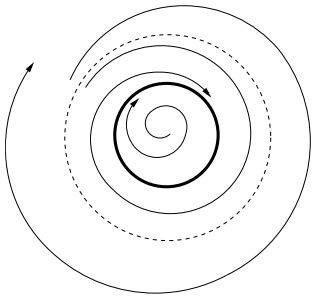

Figure 5.4: Schematic view of the presence of a stable (solid circle) and an unstable (dashed circle) limit cycle.

Let us analyze the evolution of the periodic orbit considering the diagonal $\zeta = \zeta_c$ of Figure 5.2. As the values of the parameters decrease, our simulations suggest that the stable periodic orbit is annihilated by a collision with an unstable periodic orbit. As the system of Eqs. (5.6–5.8) is a 4D system, it is impossible to represent the dynamics in the phase space similar to the case of a 2D system as in Figure 5.3. However, we give in Figure 5.4 a schematic view of the presence of the stable (solid circle) and the unstable (dashed circle) limit cycles. In Figure 5.5 we also plot the variations in time of the nondimensional radius, X, revealing the presence of the unstable orbit. Panels *a* and *b* show two limiting examples for which a slightly larger and smaller radius, respectively, than that of the unstable periodic orbit are chosen. The latter also reveals the stable limit cycle by asymptotically approaching it from larger radius. Panel *c* proves the instability of the fixed point and strengthens the existence of the stable limit cycle. In Figure 5.6 we plot also three periods of the limit cycle for the case $\gamma_c = 0.4$ and $\zeta = \zeta_c = 0.8$, where the luminosity was derived from

$$L \equiv L_r + L_c = \gamma_r X^b H^{s+4} + \gamma_c X^{-c} U_c^3. \tag{5.18}$$

The limit-cycle behavior encountered for the present model is a clear case of soft self-excited oscillations briefly mentioned in §1.2 and initially defined in Ledoux & Walraven (1958) using a model based on the Van der Pol oscillator. For such oscillations, any infinitesimal perturbation of the fixed point leads the system toward the limit cycle. Our case might be denominated *limited self-excited oscillations*, as for a perturbation stronger than a certain threshold the orbit becomes repelled by

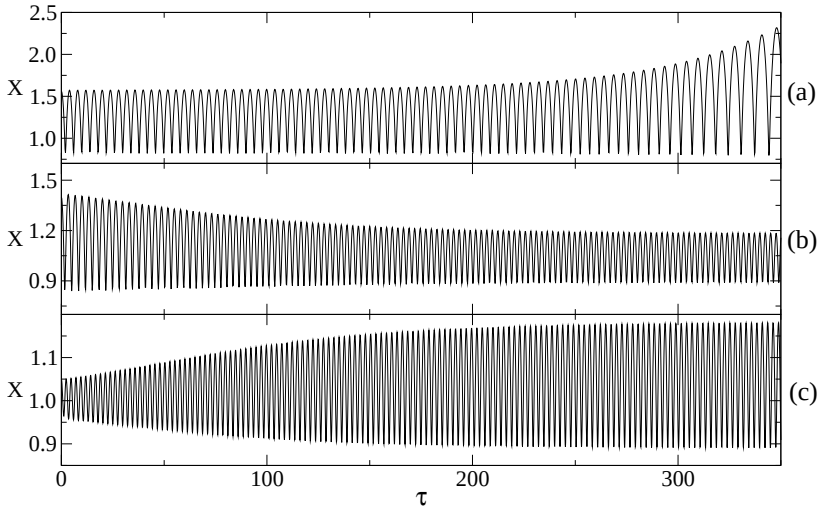

Figure 5.5: Time variations of the nondimensional radius revealing the limit cycles for $\gamma_{\rm c} = 0.4$, $\zeta = \zeta_{\rm c} = 0.8$ and several initial conditions: *(a)* $(X_0, V_0, H_0, U_{\rm c_0}) = (1.56, 0.0, 1.0, 0.7)$; *(b)* $(X_0, V_0, H_0, U_{\rm c_0}) = (1.4, 0.0, 1.0, 0.7)$; *(c)* $(X_0, V_0, H_0, U_{\rm c_0}) = (1.05, 0.0, 1.0, 0.7)$.

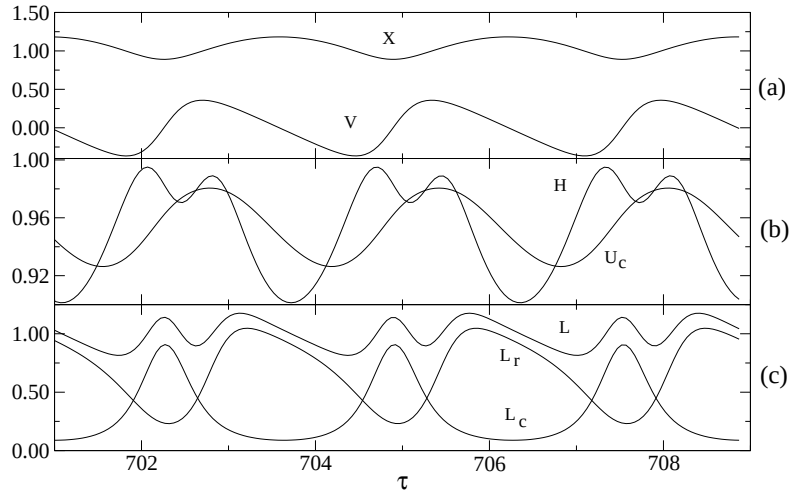

Figure 5.6: The limit cycle for $\gamma_{\rm c} = 0.4$ and $\zeta = \zeta_{\rm c} = 0.8$: *(a)* Time series of radius, X, and velocity, V; *(b)* Time variations of pressure, H, and convective velocity, $U_{\rm c}$; *(c)* Time variations of total luminosity, L, radiative luminosity, $L_{\rm r}$, and convective luminosity, $L_{\rm c}$.

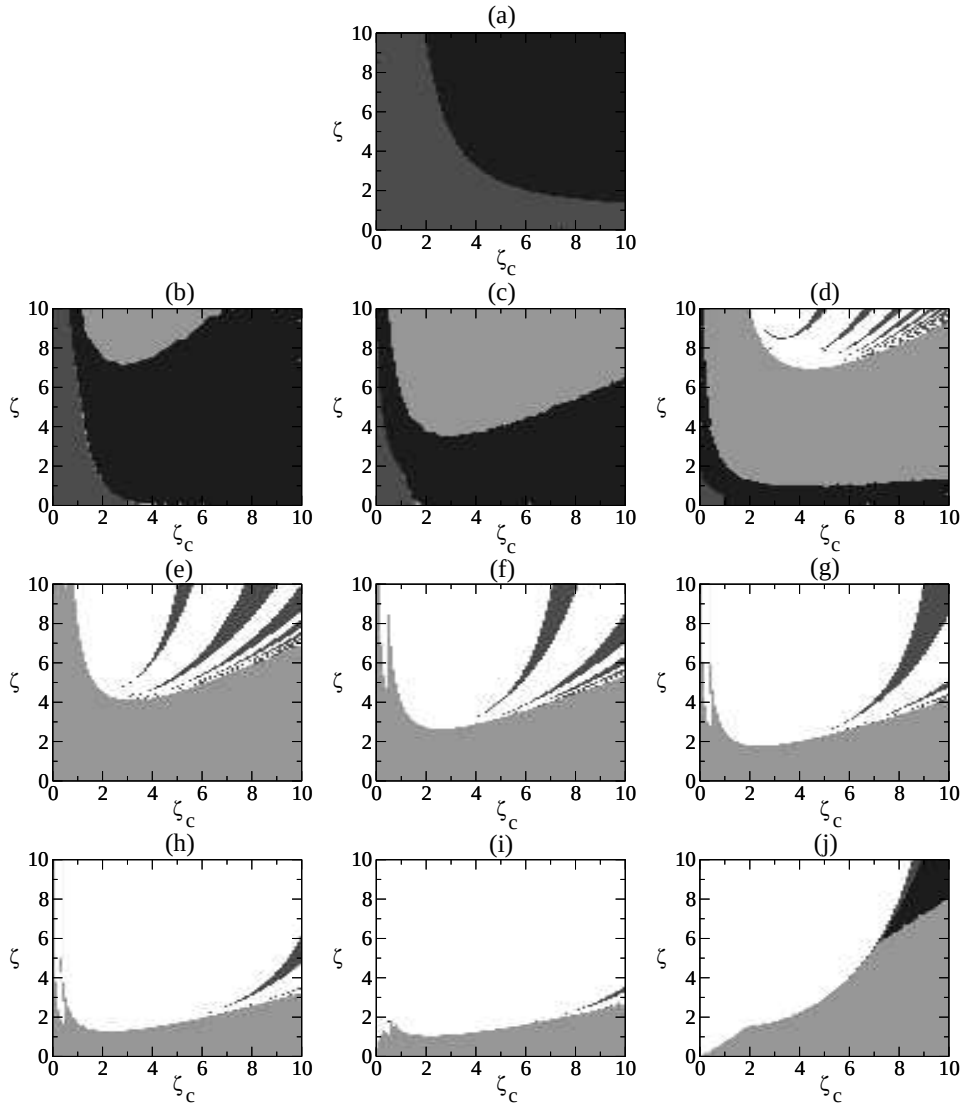

Figure 5.7: Locations of the limit cycle regions (in black) as well as stable (ligh grey) and unstable regions (dark grey) in the (ζ, ζ_c) plane for: *(a)* $\gamma_c = 0.1$; *(b)* $\gamma_c = 0.2$; *(c)* $\gamma_c = 0.3$; *(d)* $\gamma_c = 0.4$; *(e)* $\gamma_c = 0.5$; *(f)* $\gamma_c = 0.6$; *(g)* $\gamma_c = 0.7$; *(h)* $\gamma_c = 0.8$; *(i)* $\gamma_c = 0.9$; *(j)* $\gamma_c = 1.0$. The white regions represent the cases leading to singularities. See text for more details.

the unstable orbit (Figure 5.5*a*). The hard self-excited oscillations mentioned in the work of Ledoux & Walraven (1958) are better understood imagining that the limit cycles of Figure 5.4 are reversed with respect to the distance to the central fixed point — an inner unstable limit cycle and an outer stable limit cycle. In such a case, the perturbation must surpass the unstable limit cycle in order to allow the orbit to reach the stable limit cycle.

In order to see how the existence of the limit cycle is influenced by the variation of the parameters, we have performed a thorough study of the dynamics in the plane (ζ, ζ_c) for different degrees of convection γ_c. Such a search and study of the limit-cycle behavior was not followed in any of the previous investigations of the model. Moreover, the qualitative and quantitative analysis of light curves in previous studies (Stellingwerf & Donohoe 1986; Stellingwerf et al. 1987) was done only for short time series (a few dynamical times) and most crucial, for cases in which limit cycles did not exist. Therefore, we consider the search for limit cycles absolutely necessary for any further interpretation of the observed dynamics and comparison with observations.

The results are presented in Figure 5.7 showing the damping cases (in green), limit cycles (in blue) and the unstable cases divided into pulsationally unstable cases (in red) and unphysical cases in which the high values of the radius led the pressure into reaching negative values (in yellow). We have used for all cases the same value of $m = 10$ and the same initial condition, $(X_0, V_0, H_0, U_{c_0}) = (1.4, 0.0, 1.0, 0.7)$, both identical to the ones used in Stellingwerf (1986). However, the type of the resultant dynamics is independent of the initial condition as long as the latter leads to the same dynamics as any other initial condition close to the fixed point $(\bar{X}, \bar{V}, \bar{H}, \bar{U}_c) = (1, 0, 1, 1)$, a condition that we have always verified. From Figure 5.7 one can notice that in the cases dominated by radiation ($\gamma_c < 0.5$), there exist regions in the (ζ, ζ_c)-plane with stale limit cycles. As the contribution of convection to the luminosity increases and equals the contribution of radiation, the regions of limit cycles shrink and disappear completely at $\gamma_c = 0.5$. The amplitude of the limit cycle increases as one changes the values of the parameters from the green-blue edge to the blue-red edge, thus the latter also gives the values of the parameters that yield maximum amplitudes of oscillations.

Limit cycles exist only for weakly convective cases ($\gamma_c < 0.5$) which are characteristic for the classical Cepheids. However, it is worth discussing the region of limit cycles that appears for a completely convective shell ($\gamma_c = 1.0$) in Figure 5.7 and which has limit cycles of periods longer than any of the cases of smaller γ_c. Even within this approach of a simple one-zone model, it is tempting to attribute this region of the plane (ζ, ζ_c) to the instability strip of LPVs — variable red giants and supergiants — which are thought to be significantly nonadiabatic and highly convective. More exactly, the convective luminosity in the ionization regions of red pulsating variables is expected to exceed 99% of the total luminosity, as mentioned by Xiong et al. (1998a). They identify a Mira instability strip outside the Cepheid instability strip when pulsation-convection interaction is taken into account. However,

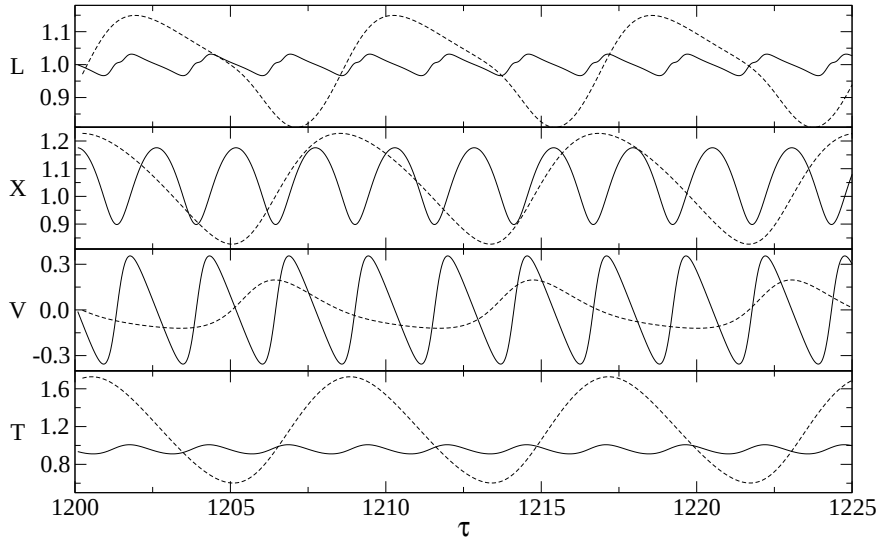

Figure 5.8: Time series for the luminosity, L, radius, X, velocity, V and temperature, T for a Cepheid-like (solid line: $\gamma_c = 0.2; \zeta_c = 1.2; \zeta = 8$) and a Mira-like star (dashed line: $\gamma_c = 1.0; \zeta_c = 9; \zeta = 7.5$).

similar to the limit cycles for the weakly convective cases possibly related to the classical Cepheids, it is highly speculative to attribute specific values of the parameters ζ and ζ_c to the cases of Miras. For comparative purposes only, in Figure 5.8 we plot the time series associated to a "Cepheid" and a "Mira" case, where the temperature was estimated from the perfect gas law as being

$$\frac{T}{T_0} = X^{-2d} H. \tag{5.19}$$

Our analysis revealed that the amplitude and period of the limit cycles depend crucially on the distance to the stability line (the blue-green frontier in the (ζ, ζ_c) plane). Approaching the unstable region from the limit-cycle region, the amplitude of the oscillations increases accompanied by an increase in the period. To exemplify this behavior, we show in Figure 5.9 a "period-luminosity" relationship in nondimensional units for the limit-cycles cases of $\gamma_c = 0.3$. The color code represents the distance, d to the blue-green stability line (Figure 5.7 *c*) calculated in the (ζ, ζ_c) plane. In Figure 5.9, ζ increases from top to bottom, while ζ_c increases from right to left. Thus, the almost-horizontal parallel lines are sequences of constant ζ, while the left-most circle of each almost-horizontal parallel line is characterized by $\zeta_c = 10$.

A more accurate analysis of this behavior reveals the fact that the morphology depends on the distance to both the stability and instability region. For example, if two cases of limit cycles, (ζ, ζ_c) and (ζ', ζ_c') are found at the same distance to the stability line, than a more pulse-like dynamics will characterize the case which is

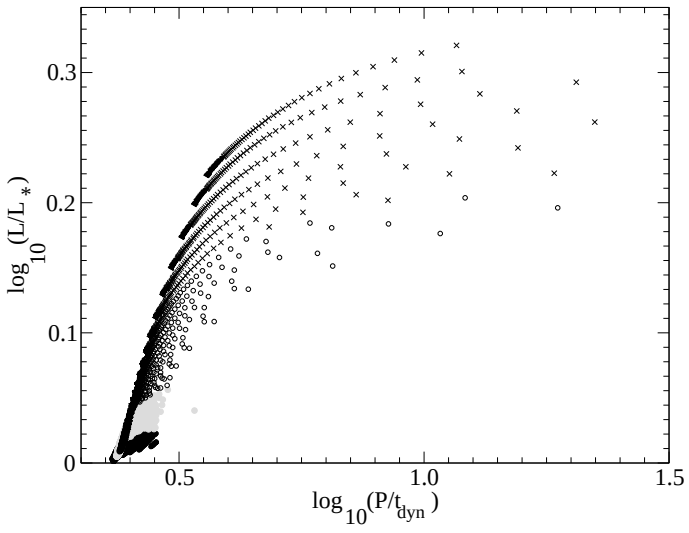

Figure 5.9: "Period-luminosity" relationship for the limit-cycle cases of $\gamma_{\rm c} = 0.3$. *(dark circles)* $0 < d < 1$; *(grey circles)* $2 < d < 2$; *(white circles)* $2 < d < 3$; *(stars)* $3 < d < 4$. See text for more details.

closer to the instability region. This makes the correlation of period, luminosity and distance to the stability/instability regions less useful for a classification of the limit cycle characteristics. Thus, another quantitative method must be found for such a purpose.

5.3 The turbulent pressure

Convection influences pulsation through three factors, namely convective energy transfer (thermodynamic coupling), turbulent pressure and turbulent viscosity (dynamic coupling). Turbulent viscosity is always a pure damping factor, whereas turbulent pressure is, in general, an excitation mechanism for stellar pulsation. Thermodynamic coupling has a damping effect in the deep layer of convective zone but it has an excitation effect at the top of the convective zones. These three factors contribute differently to pulsation with different stellar structures and pulsation modes. This fact can explain the complex pulsational character in different regions of the HR diagram — see Xiong & Deng (2001) and references therein.

The turbulent pressure, $P_{\rm t}$ is not explicitly included in Stellingwerf (1986), but it is shortly mentioned as being

$$\frac{P_{\rm t}}{P_{\rm t_0}} = X^{-m} U_{\rm c}^2, \tag{5.20}$$

where the zero subscript denotes its equilibrium value. In order to include the turbulent pressure and its associated energy terms in the one-zone approach of §5.1, one must start from the equation of momentum and energy conservation for the treatment of convection of Stellingwerf (1982):

$$\frac{D\langle \boldsymbol{u} \rangle}{Dt} = -\frac{1}{\rho}\nabla(P + P_{\rm t}) - \nabla\Phi \tag{5.21}$$

$$\frac{D}{Dt}(E + E_{\rm t}) + (P + P_{\rm t})\frac{DV}{Dt} = -\frac{1}{\rho}\nabla \cdot (F_{\rm r} + F_{\rm c} + F_{\rm t}) \tag{5.22}$$

where $D/Dt = (\partial/\partial t + \langle \boldsymbol{u} \rangle \cdot \nabla)$ is the Lagrangian time derivative, E is the specific internal energy, $V \equiv 1/\rho$ is the specific volume, P is the thermodynamic pressure and

$$E_{\rm t} \equiv \frac{1}{2}\langle (u')^2 \rangle, \tag{5.23}$$

$$P_{\rm t} \equiv \rho\langle (u')^2 \rangle, \tag{5.24}$$

$$F_{\rm c} \equiv \rho C_{\rm p}\langle (u'T') \rangle, \tag{5.25}$$

$$F_{\rm t} \equiv \frac{1}{2}\langle (\boldsymbol{u'})^2 \boldsymbol{u} \rangle \tag{5.26}$$

represent, respectively, the convective energy, the turbulent pressure, the convective and turbulent kinetic fluxes. These equations must be adapted to the one-zone model. The momentum equation translates into

$$\frac{d^2X}{d\tau^2} = (1 - \alpha_{\rm p})X^{-q}h + \alpha_{\rm p}X^{-c}U_{\rm c}^2 - X^{-2}, \tag{5.27}$$

where $q \equiv m\Gamma_1 - 2$, $c \equiv m - 2$ and

$$\alpha_{\rm p} \equiv \frac{P_{\rm t_0}}{P_0 + P_{\rm t_0}} = \frac{X_0^{-m}U_{\rm c_0}^2}{X_0^{-m\Gamma_1}h_0 + X_0^{-m}U_{\rm c_0}^2}\ . \tag{5.28}$$

To ease the calculation, the energy equation can be divided into

$$\frac{\partial(L_{\rm r} + L_{\rm c})}{\partial m} = \frac{\Gamma_1 P}{\rho^2(\Gamma_3 - 1)}\frac{\partial\rho}{\partial t} - \frac{1}{\rho(\Gamma_3 - 1)}\frac{\partial P}{\partial t} \tag{5.29}$$

$$\frac{\partial L_{\rm t}}{\partial m} = \frac{P_{\rm t}}{\rho^2}\frac{\partial\rho}{\partial t} - \frac{\partial E_{\rm t}}{\partial t}. \tag{5.30}$$

In the determination of the convective and turbulent luminosities, one can use the conservative choice of $L_{\rm c}$ of Eq.(27) of Stellingwerf (1986) and the above Eq.(5.26). The calculations lead to a formula for $L_{\rm t}$ identical to that of $L_{\rm c}$, that is $L_{\rm t} = X^{-c}U_{\rm c}^3$,

while $E_{\rm t} = U_{\rm c}^2/2$. Using Eqs.(5.29–5.30), one can get the final equation of energy conservation taking into account the turbulence:

$$\begin{aligned}\frac{dh}{d\tau} = & - m\,\frac{\alpha_{\rm p}(\Gamma_3-1)}{1-\alpha_{\rm p}}X^{2d-1}\,\frac{dX}{d\tau}\,U_{\rm c}^2 - \frac{\rho_0(\Gamma_3-1)}{P_0}\,\zeta_{\rm c}\,(X^d h^{1/2}U_{\rm c} - \\ & - X^{2d}U_{\rm c}^2) - \zeta X^{2d}\,(\gamma_{\rm r}X^b h^{s+4} + (1-\gamma_{\rm r})X^{-c}U_{\rm c}^3 - 1), \qquad (5.31)\end{aligned}$$

where $d \equiv m(\Gamma_1-1)/2$ and $\gamma_{\rm r} \equiv L_{\rm r_0}/L_0$. All the other symbols used in Eq.(5.31) have their usual meaning. The equation for the convective velocity coincides with the zero-turbulence case as the approximation made for its recovery uses of the temperature as a function of the thermodynamic pressure only.

In the case in which the turbulent energy, $E_{\rm t}$ is neglected in Eq.(5.22), Eq.(5.31) becomes

$$\begin{aligned}\frac{dh}{d\tau} = & - m\,\frac{\alpha_{\rm p}(\Gamma_3-1)}{1-\alpha_{\rm p}}\,X^{2d-1}\,\frac{dX}{d\tau}\,U_{\rm c}^2 - \\ & - \zeta X^{2d}\,(\gamma_{\rm r}X^b h^{s+4} + (1-\gamma_{\rm r})X^{-c}U_{\rm c}^3 - 1). \qquad (5.32)\end{aligned}$$

Thus, at the first approximation, the one-zone convective model with turbulent pressure is described by the Eqs. (5.27, 5.32), while the convective velocity equation remains the same from Eq.(5.8). From these equations it becomes clear that the fixed point of the new system is the same as in §5.1, $(\bar{X},\bar{V},\bar{H},\bar{U_{\rm c}}) = (1,0,1,1)$. The Jacobian of the system calculated at this fixed point is

$$J_{(1,0,1,1)} = \begin{vmatrix} 0 & 1 & 0 & 0 \\ 2-q-\alpha_{\rm p}(c-q) & 0 & 1-\alpha_{\rm p} & 2\alpha_p \\ -\zeta(\gamma_{\rm r}b-\gamma_{\rm c}c) & -\alpha_{\rm p}f & -\zeta\gamma_{\rm r}(s+4) & -3\zeta\gamma_{\rm c} \\ -\zeta_{\rm c}d & 0 & 0.5\zeta_{\rm c} & -\zeta_{\rm c} \end{vmatrix}. \qquad (5.33)$$

The secular equation obtained from the general condition for the determination of eigenvalues, $\det(\mathrm{J}_{(1,0,1,1)} - \sigma\mathrm{I}) = 0$, has the same form as Eq.(5.9), where the new parameters are

$$\begin{aligned} A &= \zeta\zeta_{\rm c}[P + RQ + 3\gamma_{\rm c}(R/2-d)] + \\ &\quad + \zeta\zeta_{\rm c}\alpha_{\rm p}[(c-q)(Q+1.5\gamma_{\rm c}) + 3\gamma_{\rm c}d + 2Qd], \qquad (5.34) \\ B &= \zeta_{\rm c}R + \zeta(P+RQ) + \alpha_{\rm p}[(c-q)(\zeta_{\rm c}+\zeta Q) + \zeta_{\rm c}(2d+f) - \zeta P], \qquad (5.35) \\ C &= \zeta\zeta_{\rm c}(Q+1.5\gamma_{\rm c}) + R + \alpha_{\rm p}[c-q+(1-\alpha_{\rm p})f], \qquad (5.36) \\ D &= \zeta_{\rm c} + \zeta Q, \qquad (5.37) \end{aligned}$$

with $P \equiv \gamma_{\rm r}b - \gamma_{\rm c}c$, $Q \equiv \gamma_{\rm r}(s+4)$, $R \equiv q-2$ and $f \equiv m(\Gamma_1-1)/(1-\alpha_{\rm p})$. The regions of stability as they result from the conditions that the real part of all

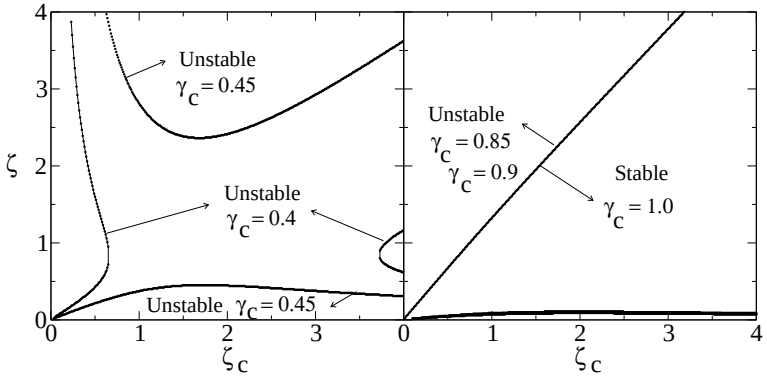

Figure 5.10: Location of pulsationally stable and unstable regions in the $(\zeta, \zeta_{\rm c})$ plane for various values of $\gamma_{\rm c}$.

eigenvalues be negative appear in Figure 5.10 represented in the spirit of Figure 5.1. One can see that the regions of stability are somewhat smaller for the cases of weak convection ($\gamma_{\rm c} < 0.5$) and significantly larger for strong convection cases. Moreover, their location is significantly different than in the case of $\alpha_{\rm p} = 0$.

As for the existence of limit cycles, we have undertaken a parametric study in order to investigate the influence of the turbulent pressure on the overall dynamics of the system and implicitly on the existence of limit cycles. For this purpose, we have chosen the same initial condition as in §5.1, that is $(X_0, V_0, H_0, U_{\rm c_0}) = (1.4, 0.0, 1.0, 0.7)$, which led to a value of $\alpha_{\rm p} \approx 0.4$. The results concerning the plane $(\zeta, \zeta_{\rm c})$ appear in Figure 5.11. As discussed in the previous section, the yellow regions represent the unphysical cases leading to negative values of the pressure and to singularity in the resulting dynamics of the system. The figures reinforce the conclusions drawn from the analysis of the secular equation. The regions characterized by the existence of limit cycle for $\gamma_{\rm c} < 0.5$ are more extended. On the other hand, in spite of the increased stability in the cases of strong convection ($\gamma_{\rm c} \geq 0.5$), the regions of nonphysical values of the variables involved (e.g., yellow regions in Figure 5.11) are more extended in these cases. The persistence of the region of stable oscillations for the completely convective case ($\gamma_{\rm c} = 1.0$) adds more reliability to its physical significance mentioned in §5.1. Compared to the case of zero-turbulent pressure, this regions shifts to smaller values of the convective efficiency, $\zeta_{\rm c}$. This shift is due to the fact that a part of the driving comes now from the turbulent pressure.

Taking into consideration the turbulent pressure certainly implies a more reliable model. However, drawing strict conclusions from the dynamics is hindered by the relatively arbitrary value of the form factor m considered in Stellingwerf (1986). There, Eq.(2.29) was used and a value of $m = 10$ was adopted. The reconsideration of this value and, moreover, of the validity of this equation makes the object of the next subsection.

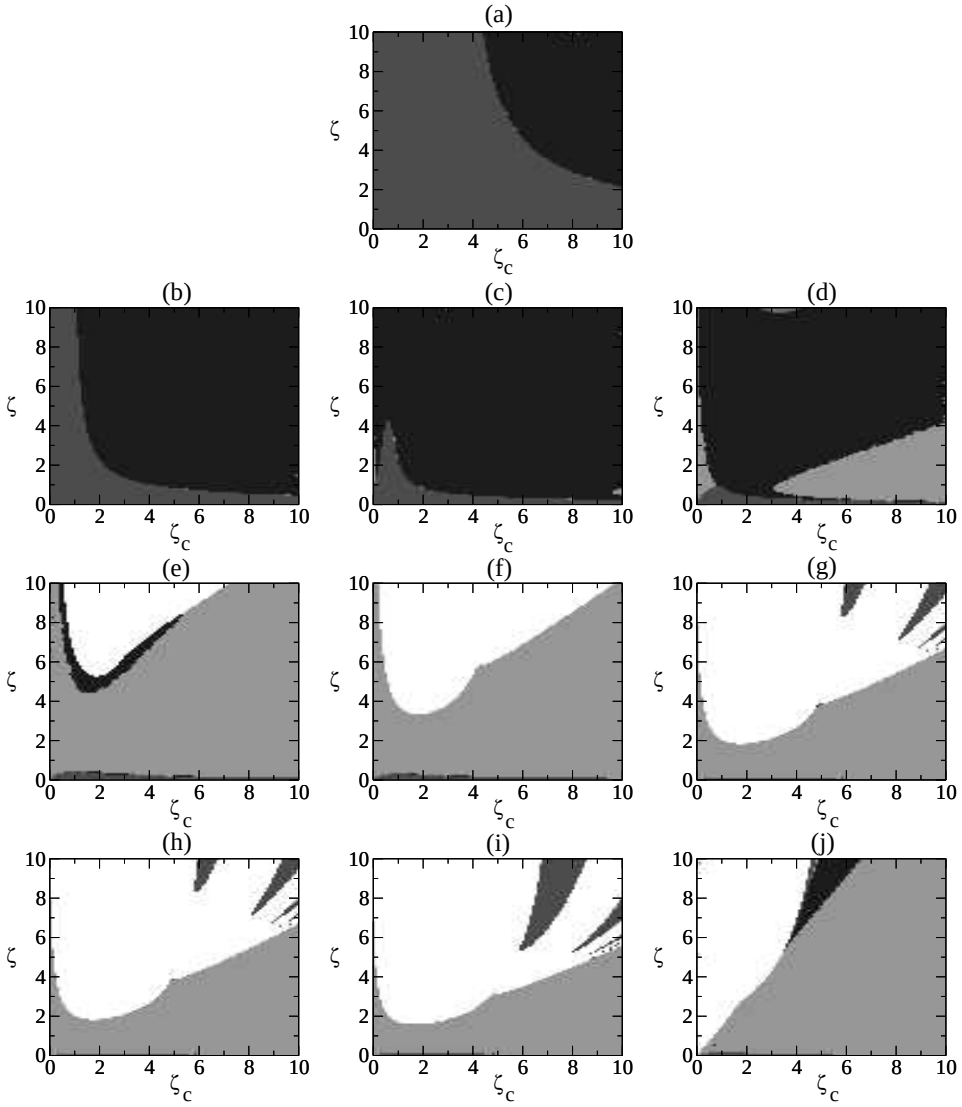

Figure 5.11: Same as Figure 5.7, but for the case in which turbulent pressure is considered.